MASTERARBEIT | MASTER'S THESIS

Titel | Title

Development of a method to assess the redox proteome

verfasst von | submitted by

Valentina Heuschneider BSc

angestrebter akademischer Grad | in partial fulfilment of the requirements for the degree of

Master of Science (MSc)

Wien | Vienna, 2026

Studienkennzahl lt. Studienblatt | Degree programme code as it appears on the student record sheet:	UA 066 862
Studienrichtung lt. Studienblatt | Degree programme as it appears on the student record sheet:	Masterstudium Chemie
Betreut von | Supervisor:	Assoz. Prof. Dr. Samuel Meier-Menches

Acknowledgements

First, I would like to express my sincere gratitude to my supervisor Sam for giving me the opportunity to conduct my master's thesis in his research group. I am very grateful for his continuous guidance, support, and valuable advice throughout this project. I learned a great deal during this time. His expertise, the many insightful discussions we had, and his constructive feedback were invaluable in shaping this work. It was a privilege to complete my master's thesis under his supervision.

I would also like to thank Andrea for generously sharing her extensive knowledge with us master's students. Her guidance, particularly in the areas of LC-MS/MS, data analysis, and cell culture, was extremely valuable.

My thanks also go to Thomas, who always seemed to have a solution whenever problems arose or experiments did not go as planned. I greatly appreciated his willingness to help and his practical advice.

A special thank you goes to Sofie, my partner in crime throughout this project. Even the longest days in the lab never felt quite so long with you around. I am very happy to have shared this experience (and the laminar) with you!

I would also like to thank the entire Meier-Menches and Gerner group, as well as my fellow master's students, for the warm welcome, the supportive atmosphere, and for always sharing their knowledge and offering help whenever needed.

Finally, I am deeply grateful to Nico for his patience, understanding, and unwavering support, especially during the more challenging times.

Abstract

Reactive oxygen species (ROS) play a central role in cellular redox processes. While controlled ROS levels participate in physiological signaling, excessive ROS generation disrupts redox homeostasis and leads to oxidative stress associated with cellular dysfunction and damage. A major mechanism through which redox signals are transmitted involves reversible oxidative post-translational modifications (oxPTMs) of cysteine residues in proteins. Due to the high reactivity of cysteine thiol groups, these residues are particularly susceptible to oxidative modifications, which can function as regulatory redox switches that modulate protein activity, structure, and interactions. Comprehensive characterization of cysteine redox states is therefore essential for understanding redox-dependent cellular regulation. The aim of this thesis was to develop, apply, and evaluate a mass spectrometry-based redox proteomics workflow to characterize cysteine-specific modifications in cellular systems and to assess how comprehensively the cellular redox proteome can be captured under defined experimental conditions. A differential alkylation strategy using N-ethylmaleimide (NEM) and isotopically labeled d5-NEM was established to distinguish between reduced and reversibly oxidized cysteine residues within a bottom-up proteomics workflow. The workflow was first validated using a defined protein mixture to assess labeling efficiency, specificity, and technical robustness, and was subsequently applied to SW480 colon carcinoma cells and Detroit 551 fibroblasts. Oxidative stress was induced using tert-butyl hydroperoxide (TBHP) and arsenic trioxide (ATO). Following treatment, whole cell lysates were subjected to differential alkylation, enzymatic digestion, and nano liquid chromatography-tandem mass spectrometry (nanoLC-MS/MS) analysis on a timsTOF Pro mass spectrometer. Proteome-wide profiling revealed treatment-dependent differences in the cellular response to oxidative perturbation. While TBHP treatment resulted in only limited proteomic alterations under the tested conditions, ATO treatment induced significant changes in protein abundance. Peptide-level analyses enabled the simultaneous assessment of cysteine redox states and protein abundance changes, indicating that redox regulation occurs in a highly site-specific manner rather than through uniform oxidation across the proteome. Combined analysis of protein- and peptide-level data examined the overlap between significantly regulated proteins and ATO-specific unique peptides, from which heat shock proteins and components of the pentose phosphate pathway were selected for detailed redox characterization. Overall, this work establishes and evaluates a differential alkylation-based redox proteomics workflow compatible with global proteome analysis and demonstrates its applicability for investigating cysteine-centered redox regulation in cellular systems. The approach provides a framework for linking cysteine-specific redox modifications with functional cellular responses to oxidative stress.

Zusammenfassung

Reaktive Sauerstoffspezies (ROS) spielen eine zentrale Rolle in zellulären Redoxprozessen. Während kontrollierte ROS-Konzentrationen an physiologischen Signalprozessen beteiligt sind, führt eine übermäßige ROS-Bildung zur Störung der Redoxhomöostase und zu oxidativem Stress, der mit zellulärer Dysfunktion und Schädigung einhergeht. Ein zentraler Mechanismus der Redoxsignalübertragung beruht auf reversiblen oxidativen posttranslationalen Modifikationen (oxPTMs) an Cysteinresten in Proteinen. Aufgrund der hohen Reaktivität von Cystein-Thiolgruppen sind diese besonders anfällig für oxidative Modifikationen, die als regulatorische Redox-Schalter fungieren können und dadurch Proteinaktivität, Struktur und Interaktionen modulieren. Eine umfassende Charakterisierung der Redoxzustände von Cysteinen ist daher entscheidend für das Verständnis redoxabhängiger zellulärer Regulationsmechanismen. Ziel dieser Arbeit war die Entwicklung und Anwendung eines massenspektrometriebasierten Redox-Proteomik-Workflows zur Analyse cysteinspezifischer Modifikationen in zellulären Systemen sowie dessen Bewertung hinsichtlich der Erfassbarkeit des zellulären Redoxproteoms unter definierten experimentellen Bedingungen. Hierzu wurde eine Differentialalkylierungsstrategie unter Verwendung von N-Ethylmaleimid (NEM) und isotopenmarkiertem d5-NEM etabliert, die eine Unterscheidung zwischen reduzierten und reversibel oxidierten Cysteinresten innerhalb eines Bottom-up-Proteomik-Ansatzes ermöglicht. Der entwickelte Workflow wurde zunächst anhand einer definierten Proteinmischung validiert, um Markierungseffizienz, Spezifität und technische Robustheit zu beurteilen, und anschließend auf SW480-Kolonkarzinomzellen sowie Detroit-551-Fibroblasten angewendet. Oxidativer Stress wurde durch tert-Butylhydroperoxid (TBHP) und Arsentrioxid (ATO) induziert. Nach der Behandlung wurden die Gesamtzelllysate differentiell alkyliert, enzymatisch verdaut und anschließend mittels Nano-Flüssigchromatographie gekoppelt an Tandem-Massenspektrometrie (NanoLC-MS/MS) auf einem timsTOF Pro analysiert. Die proteomweite Analyse zeigte behandlungsabhängige Unterschiede in der zellulären Antwort auf oxidative Perturbationen. Während die Behandlung mit TBHP unter den getesteten Bedingungen nur geringe proteomische Veränderungen zeigte, führte die Behandlung mit ATO zu signifikanten Veränderungen der Proteinabundanz. Peptidbasierte Analysen ermöglichten die gleichzeitige Untersuchung von Cystein-Redoxzuständen und Veränderungen der Proteinabundanz und zeigten, dass Redoxregulation in hohem Maße positionsspezifisch erfolgt und nicht durch eine gleichmäßige Oxidation des gesamten Proteoms beschrieben werden kann. Durch die kombinierte Analyse auf Protein- und Peptidebene der ATO-Behandlung wurde die Überlappung zwischen signifikant regulierten Proteinen und ATO-spezifischen unique Peptiden untersucht, woraus Hitzeschockproteine sowie Komponenten des Pentosephosphatwegs für eine detaillierte Redoxcharakterisierung ausgewählt wurden. Insgesamt etabliert und bewertet diese Arbeit einen auf Differentialalkylierung basierenden Redox-Proteomik-Workflow, der mit globalen Proteomanalysen kompatibel ist, und demonstriert dessen Anwendbarkeit zur Untersuchung

cysteinzentrierter Redoxregulation in zellulären Systemen. Der Ansatz ermöglicht die Verknüpfung cysteinspezifischer Redoxmodifikationen mit funktionellen zellulären Antworten auf oxidativen Stress.

Table of contents

1 Introduction

1.1 Redox biology and reactive oxygen species in cells

Reactive oxygen species (ROS) and reactive nitrogen species (RNS) comprise a chemically diverse group of oxygen- and nitrogen-derived molecules, including superoxide ($O_2^{\bullet -}$), hydrogen peroxide (H_2O_2), hydroxyl radicals ($^{\bullet}OH$) and nitric oxide ($^{\bullet}NO$), which differ markedly in reactivity, stability and biological function and contribute to cellular redox (reduction-oxidation) processes. Rather than representing a uniform class of harmful by-products, ROS are integral components of cellular redox biology,[1–3] where their steady-state levels are tightly controlled by a balance between oxidant production and antioxidant buffering systems, a concept referred to as redox homeostasis.[3,4] Within this balanced redox environment, low, regulated ROS concentrations participate in physiological signaling processes, whereas disruption of redox homeostasis results in oxidative stress characterized by excessive and uncontrolled oxidation. Thus, ROS exhibit a dual nature, acting as regulated signaling mediators under homeostatic conditions and as drivers of cellular damage when their production exceeds the cell's antioxidative capacity.[3–5]

1.1.1 Cellular sources of reactive oxygen species

Reactive oxygen species are generated by multiple intracellular sources, with mitochondria representing a major site of ROS formation due to electron transfer reactions within the respiratory chain during oxidative phosphorylation.[1,2,5,6] In addition to mitochondria, membrane-associated NADPH oxidases (NOX enzymes) constitute a dedicated and tightly regulated source of ROS, producing superoxide or hydrogen peroxide in response to cellular stimuli.[1,3,4] Further intracellular sources include peroxisomes, the endoplasmic reticulum during oxidative protein folding, and various oxidoreductase enzymes such as xanthine oxidase and cytochrome P450 systems.[1,2,5] Importantly, ROS generation by these systems is not merely a consequence of metabolic inefficiency but contributes to locally and temporally controlled physiological redox signaling.[3,4]

In addition to endogenous sources, cells may be exposed to exogenous oxidants arising from environmental factors such as air pollutants, xenobiotics and toxins, which can further perturb cellular redox balance.[5]

1.1.2 Reactive oxygen species as signaling molecules and stressors

Among reactive oxygen species, hydrogen peroxide (H_2O_2) plays a central role as a signaling oxidant due to its relative stability, controlled production and capacity for regulated diffusion within cells.[1,3,4] At low and localized levels, H_2O_2 contributes to physiological redox signaling by inducing reversible oxidative modifications of redox-sensitive amino acid residues, thereby modulating signaling pathways such as NRF2-dependent antioxidant responses, NF-κB and MAPK signaling.[1,4,5]

The specificity and reversibility of such signaling events are ensured by efficient antioxidant systems, many components of which are encoded by NRF2 target genes, including glutathione-based (GSH/GSSG redox couple) and thioredoxin-based pathways, as well as enzymatic antioxidants such as superoxide dismutases, catalase and peroxiredoxins that confine oxidant activity and preserve redox homeostasis.[1–3] When ROS production exceeds the buffering capacity of these systems, oxidative stress develops, resulting in irreversible damage to cellular macromolecules, including protein oxidation, DNA lesions, carbohydrate modification and lipid peroxidation.[1–3,5] Persistent oxidative stress and aberrant redox signaling have been implicated in the pathogenesis of numerous diseases, including cancer, cardiovascular disorders and neurodegenerative conditions, highlighting the central biological relevance of tightly regulated ROS signaling.[1,5]

1.2 Cysteine-based redox regulation and the redox proteome

The redox proteome comprises proteins that undergo reversible redox modifications as well as irreversible modifications during oxidative stress, linking cellular redox metabolism to protein structure and function.[7] Cysteine residues play a central role in redox-dependent regulation due to the unique chemical properties of their thiol (-SH) side chains.

Among amino acids present in proteins, cysteine exhibits exceptional reactivity toward oxidants and electrophiles, making it particularly sensitive to changes in the cellular redox environment.[7–9] Cysteine thiols are most reactive in their deprotonated thiolate ($-S^-$) form.[7,8] Importantly, the pKa of cysteine residues varies with the local protein microenvironment, allowing specific cysteines to exist as reactive thiolates under physiological conditions.[7,9]

Due to their reactivity, cysteine residues can undergo a diverse range of oxidative post-translational modifications (oxPTMs) that are broadly classified as reversible or irreversible, as illustrated in **Figure 1**. Reversible cysteine modifications, including sulfenylation (-SOH), disulfide formation, S-glutathionylation and S-nitrosylation, often act as regulatory redox switches that modulate protein activity, conformation and subcellular localization. These modifications are typically transient and tightly controlled, allowing redox signals to be dynamically translated into functional cellular responses.[7,10,11]

In contrast, excessive or sustained oxidative conditions can drive irreversible cysteine overoxidation to sulfinic ($-SO_2H$) or sulfonic ($-SO_3H$) acid, modifications that are generally associated with protein dysfunction, degradation or impaired regulatory capacity.[7,9–11] A prominent example of irreversible oxidative damage at the proteome level is protein carbonylation, which results from direct oxidation of amino acid side chains or secondary reactions with lipid peroxidation products and accumulates progressively during aging.[1,12]

The balance between reversible regulatory oxidation and irreversible oxidative damage is determined by both the intensity and duration of oxidant exposure, as well as the efficiency of cellular antioxidant systems. Consequently, cysteine residues act as molecular sensors that integrate redox signals while maintaining specificity and reversibility under physiological conditions.[7,9,10]

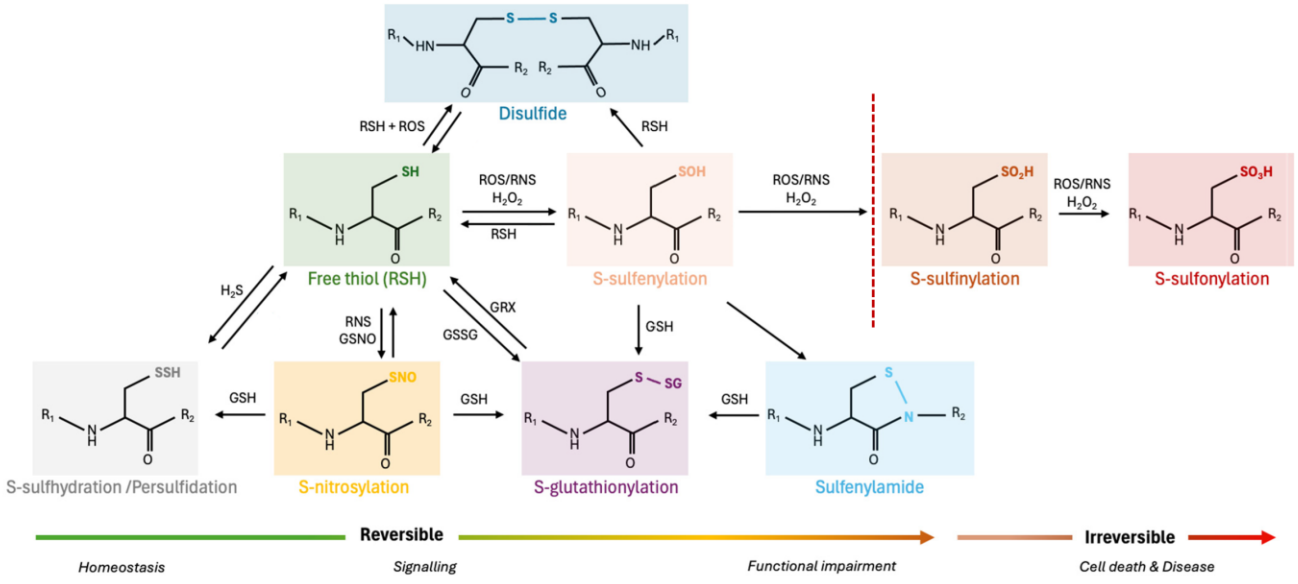

Figure 1: Overview of reversible and irreversible cysteine-based redox post-translational modifications, their interchangeability and reversibility. Figure adapted from Anjo et al.[11]

1.3 Mass spectrometry-based proteomics

Mass spectrometry (MS) has become the central analytical technology in modern proteomics, enabling large-scale identification and quantification of proteins in complex biological samples. Beyond measuring protein expression levels across conditions, MS-based proteomics enables comprehensive analysis of post-translational modifications (PTMs), providing insight into regulatory mechanisms that control protein function. The ability to localize PTMs at specific modification sites has made MS-based proteomics an essential tool for investigating cellular signaling pathways, regulatory networks, and stress-responsive processes.[8,13]

Advances in chromatography, ionization techniques, mass analyzers, and computational analysis have increased the sensitivity, depth, and throughput of proteomic experiments. Today, thousands of proteins can be routinely identified and quantified within a single experiment, covering a dynamic concentration range of more than five orders of magnitude. At the same time, this analytical complexity introduces substantial challenges, and comprehensive proteome coverage in biological systems remains a demanding task due to the wide dynamic range of protein abundances, ion suppression effects, and incomplete detection of low-abundant peptides.[13,14]

1.3.1 Principles of mass spectrometry

Mass spectrometry measures ions based on their mass-to-charge ratio (m/z). A typical mass spectrometer consists of three core components: an ion source, a mass analyzer and a detector.[13]

The ion source converts analyte molecules into gas-phase ions. The generated ions are subsequently transferred into the high vacuum of the instrument and guided to the mass analyzer, where they are separated according to their m/z ratios. Finally, the detector records the ion signals and produces a mass spectrum, which represents the relative abundance of ions as a function of their m/z ratio.[13]

1.3.2 Nano liquid chromatography (nanoLC)

High-throughput proteomics commonly employs nano liquid chromatography (nanoLC) coupled to mass spectrometry to reduce sample complexity prior to ionization and detection. NanoLC systems use columns with narrow inner diameters (≤100 µm) and operate at flow rates in the nanoliter-per-minute range, which increases sensitivity and facilitates the identification and quantification of low-abundant proteins. In proteomics, reversed-phase (RP) columns packed with silica-based C_{18} material are most frequently used, separating peptides according to hydrophobicity using an organic solvent gradient.[15,16]

To further improve chromatographic performance, nanoLC setups are typically equipped with a trap column of larger inner diameter and particle size, placed upstream of the analytical column. In an initial loading step, peptides are introduced onto the trap column at higher flow rates and under low backpressure, which concentrates retained peptides at the column head while salts and weakly retained compounds are flushed to waste.

Peptides are subsequently transferred in back-flush mode onto the analytical column for separation at nanoliter flow rates. This configuration enables injection of larger sample volumes while maintaining high separation efficiency and reducing overall analysis time.[15,16]

1.3.3 Nano electrospray ionization

Electrospray ionization (ESI) produces ions from solution by dispersing a liquid into charged droplets under a strong electric field, forming a stable Taylor cone at the emitter tip. As solvent evaporates, the droplets shrink until Coulomb repulsion exceeds surface tension (Rayleigh limit), leading to repeated droplet fission events and ultimately the release of desolvated analyte ions. ESI is a soft ionization technique and typically generates multiply charged peptide ions, which are well suited for tandem mass spectrometry.

NanoESI follows the same ionization principle but operates in a miniaturized format using very narrow emitter tips and nanoliter-per-minute flow rates. This results in smaller initial droplets, providing improved sensitivity while maintaining stable spray performance, which is particularly advantageous for proteomic applications.[17]

1.3.4 Shotgun proteomics (Bottom-up proteomics)

Shotgun, or bottom-up, proteomics is the most widely used strategy for large-scale protein profiling. In this approach, proteins extracted from cells or tissues are enzymatically digested into peptides, most commonly using trypsin, which cleaves C-terminal to lysine and arginine residues. This cleavage specificity generates peptides in an optimal mass range (average size of 700-1,500 Da)[18] for MS analysis.[19]

During MS analysis, peptides are detected in an initial MS1 scan, providing information on their m/z values and intensities. Protein identification is achieved by tandem mass spectrometry (MS/MS), in which ions are fragmented to generate MS2 spectra that are matched to theoretical fragmentation patterns derived from protein sequence databases.[19]

1.3.5 Data acquisition strategies

In proteomics, two general strategies for data acquisition using high-resolution mass spectrometry are commonly applied: data-dependent acquisition (DDA) and data-independent acquisition (DIA).[20]

In DDA, precursor ions are selected for fragmentation based on their abundances in MS1 scans. This process typically follows the top-N method, in which the N most intense precursor ions are selected for fragmentation. A dynamic exclusion list prevents repeated selection of the same precursor ions. However, because DDA preferentially samples the most abundant ions, low-abundant peptides may remain unfragmented, resulting in missing MS2 information and incomplete peptide identification.[14,20]

DIA represents a more unbiased acquisition strategy. Instead of selecting individual precursors, DIA fragments all ions within predefined m/z windows, regardless of their intensity. This reduces the loss of low-abundance peptides but generates highly complex MS2 spectra containing fragment ions from multiple precursors. Consequently, fragment ions cannot be directly assigned to a single precursor, and DIA data analysis therefore relies on spectral libraries or computationally predicted libraries, requiring more advanced bioinformatic and stringent strategies to address false-positive peptide identifications.[21,22]

1.3.6 Label-free quantitative proteomics

Protein quantification is an essential part of proteomics, enabling comparison of protein expression levels across biological or treatment conditions. Mass spectrometry-based label-free quantification (LFQ) is widely used because it does not require isotopic labeling. Two principal LFQ strategies are commonly applied: spectral count-based and peak intensity-based quantification.[14,23]

Spectral count-based quantification estimates protein abundance from the number of peptide-to-spectrum matches assigned to a protein. This approach assumes a linear MS response and is affected by differences in

peptide ionization efficiencies. Consequently, its quantitative accuracy is limited, particularly for low-abundant proteins, and it is therefore rarely used in modern proteomics.[23,24]

In contrast, peak intensity-based quantification relies on measuring peptide precursor ion intensities, typically derived from the area under the curve (AUC) of extracted ion chromatograms. This approach requires accurate alignment of retention times and mass accuracy across multiple runs. The introduction of delayed normalization, in which peptide ratios are calculated prior to scaling, has further improved quantitative accuracy by reducing systematic bias. Accordingly, intensity-based LFQ is the most commonly applied method in current proteomic workflows.[24,25]

1.3.7 timsTOF Pro™

The timsTOF Pro™ mass spectrometer (Bruker Daltonics) is a quadrupole time-of-flight (QTOF) instrument that integrates trapped ion mobility spectrometry (TIMS) as an additional gas-phase separation dimension prior to mass analysis. This configuration enables separation of ions not only by their m/z ratio but also by their ion mobility, which depends on charge state, size and molecular shape.[26,27] An overview of the instrumental configuration of the timsTOF Pro™ is shown in **Figure 2.**

Ions generated by nano-electrospray ionization using a Captive Spray source are guided through ion funnels into the TIMS tunnel.[26,27] The Captive Spray design creates a rotational airflow around the Taylor cone, which stabilizes ion formation and improves ion transmission efficiency.[28] Within the TIMS device, ions are first accumulated in a storage region. In the adjacent analysis region, ions are held stationary against a counter-flowing gas by an electric field gradient. By gradually decreasing the electric field, ions are released sequentially according to their ion mobility, with smaller and more compact ions eluting first.[26,27]

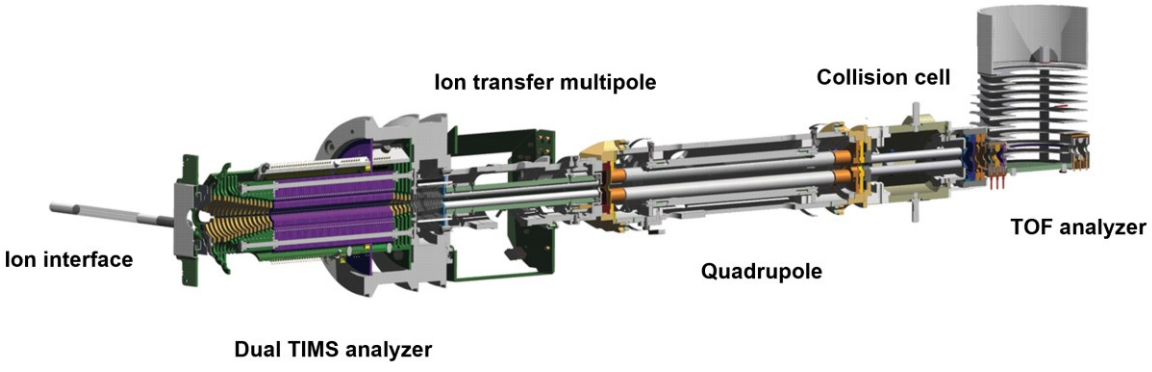

Figure 2: Schematic overview of the instrumental configuration of a timsTOF Pro. Figure adapted from Meier et al.[26]

After mobility separation, ions are transmitted into the quadrupole mass filter. Depending on the acquisition mode, the quadrupole either transmits all ions for MS1 analysis or isolates specific precursor ions for fragmentation in the collision cell. The resulting intact or fragmented ions are subsequently analysed in a two-stage reflectron time-of-flight (TOF) analyzer. In TOF mass spectrometry, ions are accelerated to the same kinetic energy and separated based on the time they require to travel a fixed distance, which depends on their mass-to-charge ratio. The reflectron compensates for small energy differences among ions of identical m/z, thereby improving mass resolution and mass accuracy while enabling fast detection. [26,27]

A key feature of the timsTOF Pro is its dual TIMS design, which allows ion accumulation and mobility analysis to occur simultaneously in separate regions of the device. This architecture forms the basis for the parallel accumulation-serial fragmentation (PASEF) acquisition strategy. In PASEF, mobility-separated ion packets are released in synchrony with rapid quadrupole switching, enabling multiple precursor ions to be fragmented within a single TIMS scan. This results in increased sequencing speed without loss of sensitivity, supporting the analysis of complex proteomic samples.[26,29]

Together, these characteristics of the timsTOF Pro™ make it particularly well suited for the analysis of complex proteomes and post-translational modifications, including redox-dependent cysteine modifications.

1.4 Methods for assessing protein redox status

While MS-based proteomics provides the technical foundation for large-scale protein and PTM analysis, the specific detection and characterization of redox-dependent modifications require specialized experimental strategies, which are discussed in the following section.

Given the central role of cysteine residues in redox regulation, redox proteomics focuses on MS-based strategies for assessing cysteine redox states. These approaches aim to preserve site-specific and quantitative information while capturing redox-driven changes in protein modification patterns and can be broadly categorized into differential alkylation, isotopic labeling, and isobaric labeling strategies.

1.4.1 Differential alkylation strategies

Differential alkylation strategies represent a well-established and conceptually fundamental approach in redox proteomics for the assessment of cysteine redox states. These methods rely on the sequential chemical discrimination of reduced and reversibly oxidized thiol groups using thiol-reactive reagents.[8,10]

Conceptually, differential alkylation involves three key steps. First, free thiols are irreversibly blocked immediately upon cell lysis using fast-reacting alkylating reagents such as N-ethylmaleimide (NEM) or iodoacetamide (IAM), thereby preserving the endogenous redox state and minimizing artificial oxidation during sample handling.[30]

Maleimide-based reagents such as NEM react selectively with cysteine thiols through nucleophilic attack of the thiolate anion on the maleimide double bond, forming stable thioether adducts (**Figure 3a**).[31] This reaction exhibits high specificity for sulfhydryl groups within a narrow pH range (pH 6.5-7.5), whereas at higher pH values increased reactivity toward amino groups may occur.[32]

In a second step (**Figure 3b**), reversibly oxidized cysteine residues - including disulfides, sulfenylated cysteines, S-glutathionylated and S-nitrosylated species (**Figure 1**) - are reduced using reagents such as dithiothreitol (DTT) or tris(2-carboxyethyl)phosphine (TCEP). While both reagents efficiently regenerate free thiols, TCEP offers advantages in redox proteomics workflows due to its irreversible reduction mechanism and higher chemical stability.[33] Following reduction, the newly reduced thiols are alkylated with a second thiol-reactive reagent that is chemically or isotopically distinct from the first, enabling mass spectrometry-based discrimination between initially reduced and oxidized cysteine populations.[8,9,30,31]

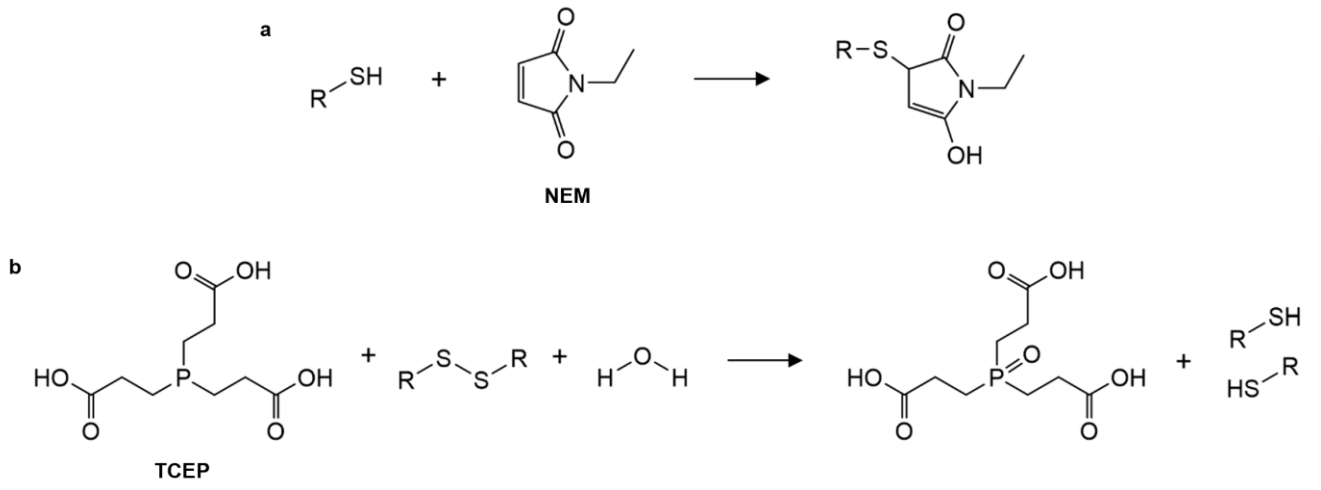

Figure 3: **a** Reaction of N-ethylmaleimide (NEM) with free thiols (-SH) and **b** reaction of the reducing agent TCEP with disulfides (-S-S-). Figure created with ChemDraw, adapted from Leichert et al.[34] and Thermo Fisher Scientific.[32,35]

A major advantage of differential alkylation approaches lies in their broad applicability, relative experimental simplicity and compatibility with global bottom-up proteomics workflows. These approaches can be readily integrated into global LC-MS/MS pipelines, enabling proteome-wide analysis while simultaneously providing site-specific information on cysteine redox states from the same dataset. This allows relative redox changes to be interpreted alongside protein abundance measurements. Furthermore, differential alkylation typically relies on widely available alkylating reagents and does not require specialized probes or instrumentation, resulting in comparatively low experimental costs and high methodological accessibility.[9,10]

Despite these strengths, differential alkylation approaches present several important limitations that require careful experimental control. Incomplete or inefficient blocking of reduced thiols during the initial alkylation step can result in free thiols being labeled in subsequent steps and falsely interpreted as oxidized cysteine residues, leading to artificial inflation of modification levels. Consequently, thiol-blocking efficiency must be empirically validated for each experimental setup.[10,30]

Moreover, differential alkylation workflows are highly susceptible to artefacts introduced during sample preparation. The high reactivity of cysteines renders them sensitive to prolonged processing times and exposure to oxygen or light, which can induce artificial oxidation or destabilize labile modifications such as sulfenic acids. Therefore, sample handling must be rapid and performed under carefully controlled conditions to minimize artefactual redox changes.[10,30] Finally, unambiguous localization of modification sites can be challenging, particularly when multiple cysteine residues are present within the same peptide.[8,30]

Despite these limitations, the differential alkylation concept forms the basis for several quantitative redox proteomics strategies, including isotopic and isobaric labeling approaches, which are discussed in the following sections.

1.4.2 Isotopic labeling strategies (OxICAT)

Isotopic labeling strategies extend the principles of differential alkylation by encoding cysteine redox states into stable isotope-resolved chemical labels.[8–10] In these approaches, cysteine-containing peptides are detected as light/heavy isotope pairs, and their relative signal intensities reflect the proportion of reduced versus oxidized cysteine residues.[8,9]

A typical isotopic labeling approach in redox proteomics is OxICAT (oxidation-dependent isotope-coded affinity tag), which combines differential thiol trapping with isotope-coded affinity tags.[9,34] In OxICAT workflows, nascent thiols are first alkylated with a “light” ICAT reagent, whereas reversibly oxidized cysteines are reduced and subsequently labeled with a chemically identical but isotopically “heavy” ICAT reagent.[34] The ICAT reagent consists of a cysteine-reactive IAM-group, a stable isotope-encoded linker, and a biotin affinity handle.[36] Following proteolytic digestion, ICAT-labeled peptides are selectively enriched by streptavidin-biotin affinity chromatography prior to MS analysis, thereby reducing sample complexity and enhancing detection of cysteine-containing peptides.[9,10]

A major strength of isotopic labeling strategies lies in their ability to provide quantitative ratios of reduced and oxidized cysteine residues based on the relative MS1 intensities of light and heavy peptide pairs.[34] However, OxICAT also presents notable limitations. The requirement for affinity enrichment restricts analysis to ICAT-labeled cysteine-containing peptides, thereby reducing overall proteome coverage and limiting simultaneous global

protein profiling. In addition, although affinity-based enrichment improves selectivity, the associated multiple sequential sample preparation steps increase the risk of sample loss and introduce additional sources of technical variability. The method further relies on specialized reagents and comparatively complex workflows, resulting in increased experimental cost and reduced throughput, particularly in studies involving multiple experimental conditions or replicates.[8–10]

Despite these constraints, OxICAT remains a benchmark method for quantitative thiol redox proteomics and has demonstrated that many cysteine residues are partially oxidized even under steady-state conditions.[37]

1.4.3 Isobaric labeling strategies (TMTs)

Isobaric labeling strategies represent a more recent advancement in quantitative proteomics, aiming to increase throughput and experimental scalability by enabling multiplexed analysis. These approaches use tandem mass tags (TMTs) to encode multiple samples with chemically distinct but isobaric tags, allowing their simultaneous analysis within a single mass spectrometry run. Quantitative information is obtained from sample-specific reporter ions that are released upon peptide fragmentation during MS/MS.[9,10,14]

In redox proteomics, iodoTMT reagents integrate thiol-reactive chemistry with isobaric mass tagging. iodoTMT tags consist of three functional elements: a cysteine-reactive IAM-group, a mass normalizer region that ensures all labeled peptides are isobaric at the MS1 level, and a low-mass reporter group for sample-specific quantification at the MS2 level.[14,38]

In iodoTMT-based workflows, free thiols are first alkylated with one set of iodoTMT reagents, followed by reduction and labeling of newly reduced thiols with a second set of iodoTMT reagents.[39] Labeled samples are pooled prior to MS/MS analysis, enabling simultaneous quantitative comparison of cysteine redox states across samples.[8,10,39]

A key advantage of isobaric labeling strategies is their high degree of multiplexing, with current TMT formats enabling simultaneous analysis of up to 11, 16, or 18 samples within a single experiment. Because all samples are combined and analyzed together, reporter ion intensities are measured under identical chromatographic and instrument conditions, thereby minimizing run-to-run variability and improving quantitative reproducibility. Moreover, TMT-based redox proteomics is compatible with global proteomics workflows, allowing parallel assessment of cysteine redox changes and protein abundance from the same dataset.[9,14]

However, TMT-based redox proteomics is constrained by high reagent costs and the requirement for careful experimental design. In addition, quantitative accuracy can be compromised by reporter ion ratio compression resulting from co-isolation and co-fragmentation of near-isobaric contaminant ions, particularly in complex samples.[8,10,14]

Overall, isobaric labeling strategies provide multiplexed, high-throughput analysis of cysteine redox dynamics and are particularly well suited for comparative studies across multiple experimental conditions and large sample cohorts.

1.5 Chemical induction of oxidative stress in cell systems

Controlled induction of oxidative stress in cells represents a central experimental strategy for investigating redox-dependent cellular responses and evaluating the performance of redox proteomics workflows. Chemical oxidants are commonly employed to perturb cellular redox homeostasis in a reproducible and tunable manner for systematic analysis of redox-regulated protein modifications under defined stress conditions.[40,41]

Tert-butyl hydroperoxide (TBHP) is frequently used for the induction of oxidative stress in cell-based systems as a direct oxidative agent. Unlike H_2O_2, which is a small, water-soluble oxidant that rapidly diffuses throughout the cell and can lead to widespread oxidation, TBHP is a lipophilic peroxide that preferentially targets membrane-associated structures and lipid-rich cellular compartments, including mitochondrial membranes.[40,41]

In contrast, arsenic trioxide (ATO) induces oxidative stress predominantly through indirect mechanisms that promote intracellular reactive oxygen species formation.[42,43] Instead of acting as a direct oxidant or eliciting a uniform, global ROS burst, ATO perturbs cellular redox regulation and promotes lipid peroxidation, leading to the accumulation of reactive aldehydes that act as longer-lived mediators of oxidative damage.[44] ATO therefore represents a mechanistically distinct oxidative stressor that complements peroxide-based models and enables investigation of ROS generation arising from disrupted redox regulation.

2 Aims and Objectives

The cellular redox proteome comprises proteins whose function and regulation are modulated by redox-active processes, with cysteine thiol groups playing a central role in redox regulation. Reversible oxidation of cysteine residues can act as regulatory, thiol-based switches controlling protein activity and interaction, whereas prolonged or excessive oxidative stress may promote irreversible cysteine oxidation associated with cellular dysfunction and damage.[7] Comprehensive analysis of cysteine-based oxidative post-translational modifications is therefore essential for understanding redox regulation in physiological and pathophysiological contexts.

The primary aim of this work is to develop, apply, and evaluate a mass spectrometry-based workflow for the analysis of cysteine-specific redox modifications in cells, with the objective of identifying parameters that describe how comprehensively and reliably the cellular redox proteome was captured under defined experimental conditions.

To achieve this aim, a differential alkylation strategy using N-ethylmaleimide (NEM) and isotopically labeled d5-NEM is established and assessed. This approach was selected as it provides a balanced compromise between proteome coverage, quantitative sensitivity, and methodological simplicity. In contrast to cysteine-specific affinity enrichment strategies, the applied workflow enables global proteome analysis while reducing potential enrichment-related biases and sample loss. This choice is further supported by high abundance of cysteine residues in the human proteome, with approximately 214,000 cysteine residues encoded in the human genome,[7] resulting in a substantial number of cysteine-containing peptides that remain detectable even in unenriched samples. Moreover, the use of widely available reagents, low experimental costs, and straightforward sample handling facilitates seamless integration into standard bottom-up proteomics workflows.

The workflow is first validated using a defined protein mixture to evaluate labeling efficiency, specificity, and technical robustness. Subsequently, the method is applied to fibroblast and colon carcinoma cell lines to assess redox proteome coverage in biologically relevant cellular systems.

ROS-stress and inflammatory stimulation are employed as experimental perturbations. Oxidative stress is induced using tert-butyl hydroperoxide (TBHP) and arsenic trioxide (ATO), while inflammatory signaling is stimulated by interleukin-1β (IL-1β) treatment. These perturbations are used to evaluate whether distinct stress mechanisms are reflected in measurable changes within the captured redox proteome.

Cysteine-based redox information is analysed at both protein and peptide level to distinguish redox-driven effects from changes in protein abundance. Based on these analyses, parameters such as the extent of cysteine modification, site specificity, reproducibility and responsiveness to redox and inflammatory perturbations are derived to describe the quality and coverage of the redox proteome captured by the established workflow.

Overall, this thesis integrates aspects of cell culture, sample preparation and LC-MS/MS data acquisition to establish and evaluate a differential alkylation-based redox proteomics workflow. In parallel, complementary data analysis strategies are applied to relate methodological parameters to biologically meaningful readouts.

3 Material and Methods

All used materials and devices are listed in **Table 14** in the appendix.

3.1 Cell culture

3.1.1 Cell lines

For redox proteome profiling two different adherent cells lines were used. The colon carcinoma cell line SW480 and the fibroblast cell line Detroit 551 were obtained from American Type Culture Collection (ATCC) (**Figure 4**).

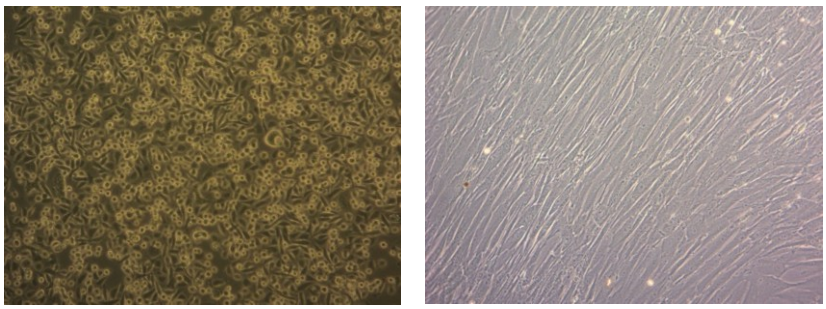

Figure 4: SW480 colon carcinoma cells (right) and Detroit 551 fibroblasts (left) in culture under the microscope.

Both, SW480 and Detroit 551 cells were cultured in Eagle's Minimum Essential Medium (MEM, Sigma Aldrich) supplemented with 10% (v/v) heat inactivated fetal bovine serum (FBS, Gibco) and 1% (v/v) penicillin-streptomycin (1000 units penicillin, 10 mg·mL^{-1} streptomycin, Sigma Aldrich). Cells were maintained in T75 flasks with ventilated caps (Sarsted AG & Co. KG) and grown in Heracell 150i CO_2 incubator (Thermo Fisher Scientific) at 37 °C in a humidified atmosphere containing 5% CO_2.

3.1.2 General Procedures

Cells were routinely subcultured upon reaching approximately 80% confluency. Cell morphology and confluency were checked every second day using a Primo Vert microscope equipped with an AxioCam ERc5s camera and Zen 2011 (blue edition v1.0.0.0) software (ZEISS AG).

For subculturing, spent medium was first removed, followed by a washing step with 5 mL phosphate-buffered saline (PBS; composition listed in **Table 1**). After removal of PBS, 3 mL of 0.25% Trypsin/EDTA solution (Sigma Aldrich) were added, and the cells were incubated for approximately 5 min to allow complete detachment from the flask surface. Trypsinization was stopped by adding 7 mL of fresh culture medium. The cell suspension was mixed thoroughly by gentle pipetting and transferred to 15 mL polypropylene tubes (Falcon, Corning).

Cells were pelleted by centrifugation in a Megafuge 16R centrifuge (Thermo Scientific) for 5 min at 1100 rpm and 23 °C (ACC = 9, DEC = 9). The supernatant was discarded, and the cell pellet was resuspended in fresh culture medium, typically in a final volume of 1 mL. Defined ratios of the cell suspension were subsequently transferred to new culture flasks containing fresh medium. For routine medium exchange, spent medium was removed and replaced with fresh medium.

Table 1: Composition of PBS buffer (phosphate buffered saline) pH 7.4.

Compound	Concentration [mM]
NaCl	137
KCl	2.7
Na_2HPO_4	10
KH_2PO_4	1.8
Water	-

For long-term storage, cells were cryopreserved in liquid nitrogen using 10% (v/v) dimethyl sulfoxide (DMSO, Sigma Aldrich) in MEM as a cryoprotective agent. Cells were trypsinized as described above, pelleted by centrifugation, and resuspended in cryoprotective medium. Aliquots of 1 mL cell suspension were transferred into cryovials and placed in a cryo-box. Cells were frozen by gradual temperature reduction, initially at -80 °C and subsequently transferred to liquid nitrogen at -196 °C, allowing controlled dehydration prior to freezing.

For thawing, cryovials were rapidly warmed in a 37 °C water bath for approximately 2 min to minimize ice recrystallization. Immediately after thawing, the cell suspension was transferred to a 15 mL tube containing 9 mL of pre-warmed fresh medium and centrifuged for 5 min at 1100 rpm to remove residual DMSO. The supernatant was discarded, and cells were resuspended in 1 mL fresh medium before seeding into T75 culture flasks containing 10 mL medium that had been pre-equilibrated at 37 °C.

3.1.3 Cell counting

Cell counts were performed using an automated cell counter with brightfield imaging technology (DeNovix CellDrop BF) based on trypan blue exclusion. For SW480 cells, suspensions were diluted 1:10 with phosphate-buffered saline by mixing 10 µL cell suspension with 90 µL PBS. Subsequently, 100 µL of 0.4% trypan blue solution (Sigma-Aldrich) were added, and 10 µL of the resulting mixture were pipetted onto the alignment groove of the device's optical surface for analysis.

The same procedure was applied for Detroit 551 cells, except that no prior dilution was required. In this case, 20 µL of cell suspension were mixed directly with 20 µL of 0.4% trypan blue solution. Cell-specific counting protocols were programmed on the device to account for differences in cell morphology, including cell roundness, diameter and experimental dilution factors. Exposure settings were checked prior to each measurement and adjusted if necessary using the device touchscreen.

3.1.4 MTT cytotoxic assays

To assess cell viability and proliferation of SW480 and Detroit 551 cells upon tert-butyl hydroperoxide (TBHP) and arsenic trioxide (ATO) treatment, a colorimetric MTT (3-(4,5-dimethylthiazol-2-yl)-2,5-diphenyltetrazolium bromide) assay was performed in standard 96 well plates (Sarsted AG & Co. KG). To minimize evaporation effects, the outermost wells were filled with 100 µL PBS. Cells were seeded in densities of 10,000 cells per well in 100 µL Eagle's Minimum Essential Medium and allowed to adhere for 24 h under standard culture conditions. Wells containing medium only were prepared as blanks.

Cells were treated by adding 100 µL of TBHP or ATO solutions at the indicated concentrations, while MEM medium served as negative control and blank. For each compound concentration, three or six technical replicates were performed. Following 24 h incubation, 20 µL MTT reagent (Sigma Aldrich, 5 $mg \cdot mL^{-1}$ in PBS) were added to each well (10% v/v), and plates were incubated for an additional 3 h. Subsequently, the supernatant was removed, and the resulting formazan crystals were dissolved in 100 µL DMSO.

Absorbance was measured at 570 nm using a Multiskan GO photometric plate reader controlled via SkanIt software (v.3.2.0.35 Research Edition; Thermo Fisher Scientific). Raw data were processed in Microsoft Excel. All values were blank corrected by subtracting the average blank absorbance, and cell viability was normalized to the averaged absorbance of untreated control samples. Normalized viability data were analyzed in GraphPad Prism using nonlinear regression with the "log(inhibitor) vs normalized response - Variable slope" model. Half maximal inhibitory concentrations (IC_{50}) were calculated from the resulting sigmoidal dose-response curves.

MTT assays were performed using TBHP concentrations ranging from 6.8 µM to 1000 µM for both Detroit 551 and SW480 cells. In addition, ATO-induced viability effects were assessed in SW480 cells using concentrations between 7.8 µM and 100 µM.

3.1.5 Stock solutions

Stock solutions for treatments were prepared as follows: Tert-butyl hydroperoxide (TBHP, 70% w/w in H_2O, Sigma Aldrich) was diluted in sterile-filtered phosphate-buffered saline (PBS) to obtain stock solutions of 100 mM and 10 mM.

Human recombinant interleukin-1β (IL-1β, ≥ 98%, Sigma Aldrich) was prepared as a 100 µg·mL^{-1} stock solution in sterile-filtered PBS, from which a 10 µg·mL^{-1} working solution was generated by dilution. Arsenic trioxide (ATO, Sigma Aldrich) was dissolved in VWR water supplemented with NaOH to prepare a 48 mM stock solution.

For preliminary protein mixture experiments, ubiquitin, cytochrome c, albumin, and thioredoxin reductase 1 were each prepared as 1 µg·µL^{-1} stock solutions in water (all Sigma).

3.2 Cell-free assessment of redox status

To validate the differential alkylation strategy using N-ethylmaleimide (NEM) and d5-NEM for assessing protein redox status, the experimental design was first evaluated using a defined protein mixture. The workflow was adapted from a published approach [45] and optimized for subsequent cell-based experiments. An overview of the experimental workflow is shown in **Figure 5**.

A protein mixture consisting of ubiquitin, cytochrome c, albumin, and thioredoxin reductase 1 (TXNRD1) was used for method validation. Individual stock solutions (1 µg·µL^{-1}) were prepared, and 5 µL of each were combined to yield a total protein amount of 20 µg. The mixture was adjusted to a final volume of 90 µL using 50 mM ammonium bicarbonate buffer (ABC, pH 7.2, Sigma Aldrich).

The differential redox digestion was performed as described in section 3.4.3. Briefly, free thiols were first alkylated with NEM, followed by reduction of reversibly oxidized cysteine residues and subsequent labeling with isotopically labeled d5-NEM, followed by protein digestion and LC-MS/MS analysis. Filtration steps were included to remove excess reagent between labeling reactions.

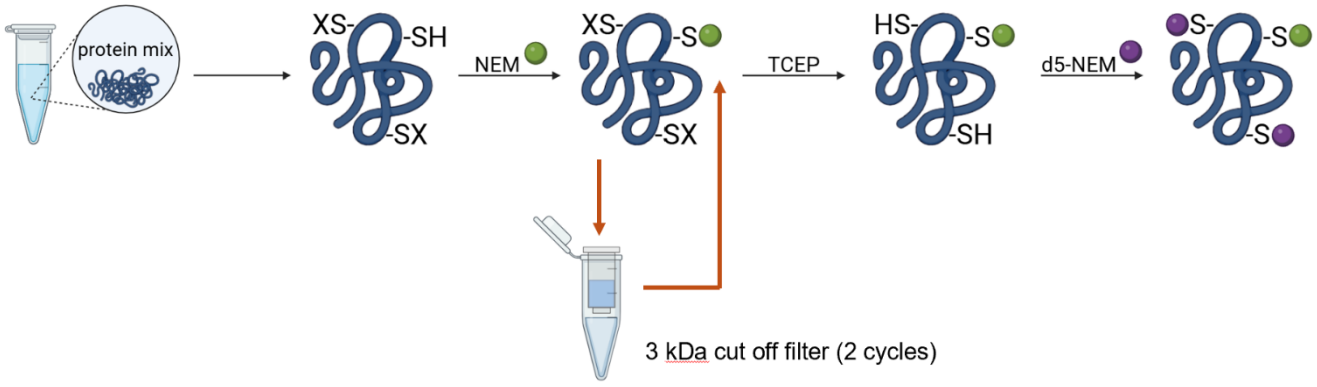

Figure 5: Schematic overview of the differential alkylation workflow used for redox proteomics method development. Free cysteine residues are initially blocked using NEM, followed by reduction of reversibly oxidized thiols and labeling with isotopically labeled d5-NEM. Filtration steps using cut-off filter are applied between reactions to remove excess reagents. Figure created with Biorender, adapted from Hoehlschen et al.[46]

3.3 Redox proteomics *in vitro*

For the final redox proteomics experiments, SW480 cells at passage 25 and Detroit 551 cells at passage 17 were used. Redox proteomic profiling experiments were performed in 6-well plates (Sarstedt AG & Co. KG). Cells were counted and seeded in densities of 250,000 cells per well in 2 mL culture medium and allowed to adhere for 24 h prior to treatment. All experimental conditions were performed in four biological replicates. An overview of the final cell-based redox proteomics workflow is shown in **Figure 6**. Briefly, following treatment, cells were harvested as whole cell lysates. Protein concentrations were determined and normalized prior to differential alkylation of cysteine residues using NEM and d5-NEM. Proteins were subsequently digested with Trypsin/Lys-C, desalted, and analysed by LC-MS/MS.

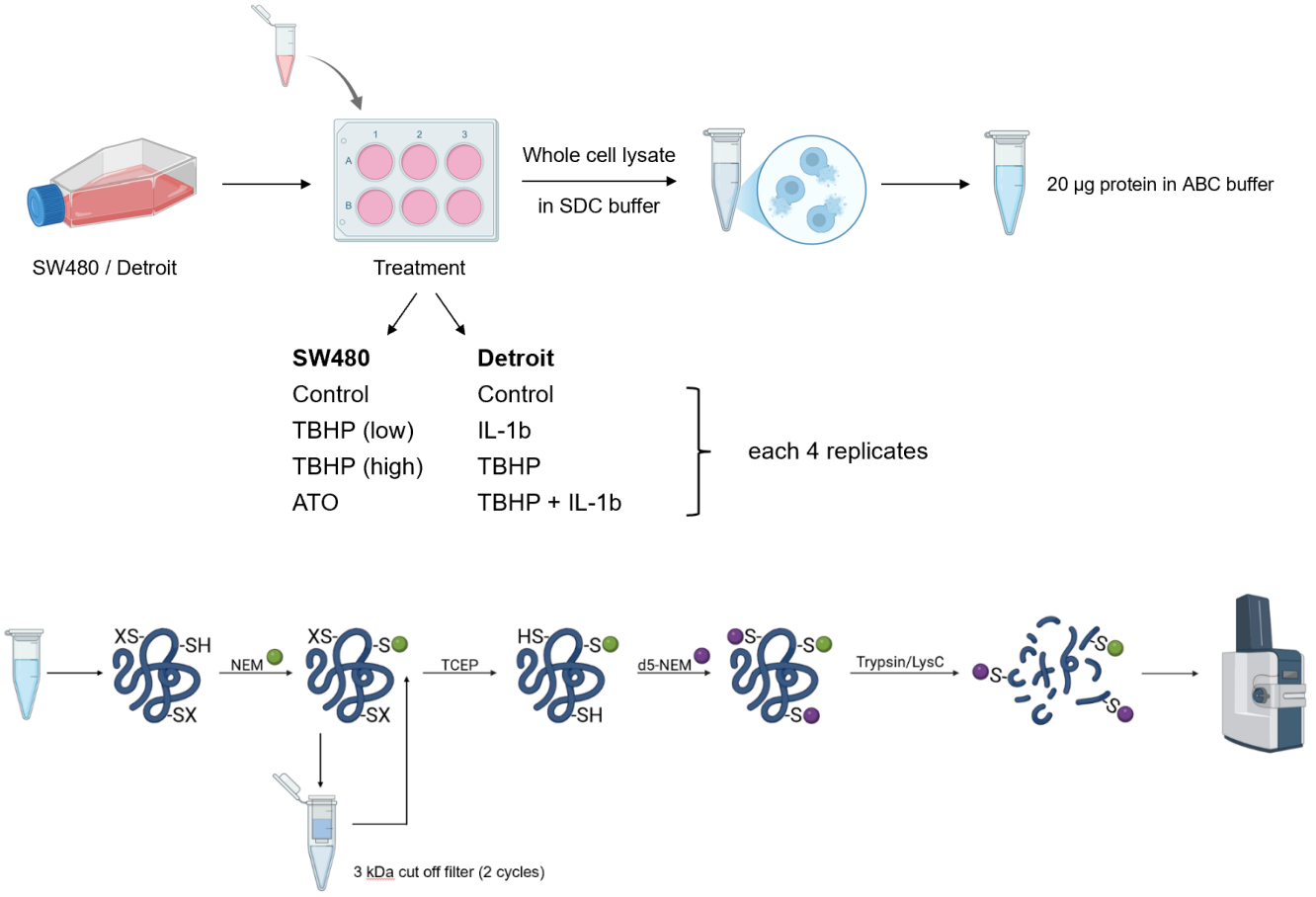

Figure 6: Overview of the final cell-based redox proteomics workflow. SW480 and Detroit 551 cells were treated as indicated, lysed, and subjected to differential alkylation of cysteine residues using NEM and d5-NEM, with intermediate removal of excess reagents using cut-off filters, followed by proteolytic digestion and LC-MS/MS analysis. All conditions were analyzed in four biological replicates. Figure created with Biorender.

3.3.1 Treatment of SW40 colon cancer cells

SW480 cells were treated with 15.6 µM or 62.5 µM tert-butyl hydroperoxide (TBHP) or 5 µM arsenic trioxide (ATO). For treatment, 1 mL medium was removed from each well and replaced with 1 mL of fresh medium containing the respective treatment compound. Control cells were treated with fresh culture medium containing an equivalent volume of PBS corresponding to the highest treatment concentration

After 24 h cells were processed and collected as whole cell lysates as described in section 3.4.1.

3.3.2 Treatment of Detroit 551 fibroblast cells

Detroit 551 cells were treated with 60 µM TBHP and 10 $ng \cdot mL^{-1}$ interleukin 1β (IL-1β), applied either as single treatments or in combination. TBHP treatment was performed by removing 1 mL medium and adding 1 mL treatment solution prepared in fresh culture medium. For control wells and IL-1β-only treatment, a medium change with 1 mL fresh culture medium was performed. Control medium contained an equivalent PBS volume corresponding to the highest treatment concentration.

For IL-1β treatment, 200 µL of a 10 $\mu g \cdot mL^{-1}$ stock solution (in PBS) were added to the wells 1 h after TBHP treatment Cells were incubated for an additional 3 h, resulting in a total incubation time of 4 h. Subsequently, cells were processed and collected as whole cell lysates as described in section 3.4.1.

3.4 Sample preparation

3.4.1 Whole cell lysates

After completion of the incubation period, the 6-well plates were placed on ice for sample collection. The culture medium was removed, and each well was washed twice with 1 mL of ice-cold PBS buffer. Following removal of PBS, cells were detached by scraping twice using a cell scraper (Sarstedt AG & Co. KG), with the sequential addition of freshly prepared sodium deoxycholate (SDC, Sigma; composition listed in **Table 2**) lysis buffer (80 µL for the first scrape and 50 µL for the second).

Whole cell lysates were collected in Eppendorf tubes after each lysis step and immediately incubated at 95 °C and 1400 rpm for 5 min in a thermoshaker (Eppendorf AG, Thermomixer comfort) to ensure efficient protein solubilization and denaturation. Samples were then allowed to cool to approximately room temperature and briefly centrifuged to remove condensate and either stored at -20 °C or processed directly for protein quantification.

Table 2: Composition of SDC lysis buffer.

Compound	Concentration [mM]
Sodium deoxycholate ≥ 98%	102
TRIS (Tris(hydroxymethyl)-aminomethane)-HCl pH 8.5	100
Water	-

3.4.2 Protein quantification by Bicinchoninic acid (BCA) colorimetric assay

Total protein concentrations of whole-cell lysates were determined using a colorimetric bicinchoninic acid (BCA) assay to enable normalization of sample amounts prior to protein digestion. Samples stored at -20 °C were thawed at room temperature and briefly centrifuged in a tabletop centrifuge (Eppendorf AG, Centrifuge 5425 R). Lysates were transferred to 15 mL Falcon tubes and sonicated using an Ultrasonic Stick (Bandelin) for 1 s at 90% power, repeated three times per sample. Falcon tubes were centrifuged for 2 min at 100 g to collect the liquid at the bottom and samples were subsequently transferred back into Eppendorf tubes. Samples were then incubated at 95 °C and 300 rpm for 5 min in a preheated thermoshaker (Eppendorf AG, Thermomixer C), allowed to cool to room temperature, and briefly centrifuged at high speed to remove condensate from the tube lids.

For calibration, ten BCA standards were prepared in a 96-well plate by combining 0 - 9 µL of a 1 µg/µL bovine serum albumin (BSA, Carl Roth GmbH + Co. KG)) solution with 0 - 9 µL VWR water and 1 µL SDC to a final volume of 10 µL. Sample wells were prepared by mixing 9 µL VWR water with 1 µL of sample. The photosensitive working reagent was freshly prepared by mixing reagent A (Table 3; 29 mM bicinchoninic acid, 188.7 mM sodium carbonate, 8.25 mM sodium tartrate, 113 mM sodium bicarbonate, pH 11.25) with reagent B (200 mM $CuSO_4 \cdot 5H_2O$) in a 50:1 ratio. Subsequently, 200 µL of working reagent were added to each well.

Plates were covered with aluminum foil to protect from light, shaken for 1 min at 800 rpm on a tabletop mixer, and incubated at 40 °C for 45 min. Absorbance was measured at 562 nm using a photometric plate reader. Raw data were exported to Microsoft Excel, where absorbance values of the BSA standards were plotted against protein concentration. Protein concentrations of the samples were calculated using linear regression of the calibration curve.

Table 3: Composition of reagent A (100 mL, pH 11.25) and reagent B (10 mL in water) for BCA assay.

	Compound	Concentration [mM]
Reagent A	Bicinchoninic acid	29
	Sodium carbonate	188.7
	Sodium tartrate	8.25
	Sodium bicarbonate	113
	Water	-
Reagent B	Copper Sulfate · $5H_2O$	200

3.4.3 In-solution redox digestion protocol

Based on protein concentrations determined by BCA assay, samples were diluted to 20 µg total protein using ammonium bicarbonate buffer (ABC, 50 mM in water pH 7.2) and adjusted to a final volume 90 µL. For the protein mixture pre-experiments, no protein quantification was required, and samples were directly adjusted to a final volume of 90 µL with ABC buffer.

After a brief centrifugation step, 2 µL N-ethylmaleimide (NEM, Sigma Aldrich) from a 100 mM stock solution were added to each sample, resulting in a final concentration of 2.2 mM. Samples were immediately vortexed and incubated at 23 °C and 1200 rpm for 20 min in a thermoshaker (Eppendorf AG, Thermomixer comfort) to alkylate free thiol groups.

To remove excess NEM prior to reduction, samples were transferred to VivaSpin® 500 µL centrifugal filter units (Sartorius, 3 kDa molecular weight cut-off) after a short centrifugation step. Spin columns were filled to 400 µL with ABC buffer (50 mM pH 7.2) and centrifuged at 15,000 g and 20 °C in a tabletop centrifuge (Eppendorf AG) until sample volume was reduced to approximately 20 - 30 µL. This filtration step was repeated once by refilling the columns to 400 µL with ABC buffer centrifuging under identical conditions. Each centrifugation cycle lasted about 1.5 - 2 h. After the second filtration step, ABC buffer was added to restore a final sample volume of 90 µL, and samples were transferred back into the corresponding Eppendorf tubes

For the first protein mixture pre-experiment, the centrifugal filtration step was omitted. As part of workflow optimization, the cut-off filters were introduced in a second protein mixture experiment to reduce residual NEM prior to the reduction step.

Subsequently, 5 µL of 100 mM Tris(2-carboxyethyl)phosphine hydrochloride (TCEP, Sigma Aldrich) from a 100 mM stock solution were added to each sample, resulting in a final concentration of 5 mM. Samples were vortexed immediately and incubated at 45 °C and 1200 rpm for 20 min in a thermoshaker to reduce reversibly oxidized cysteine residues.

After a brief centrifugation step to collect the sample, 5 µL of isotopically labeled N-d5-ethylmaleimide (d5-NEM; Sigma-Aldrich) from a 200 mM stock solution were added, resulting in a final concentration of 10 mM. Samples were vortexed and incubated for an additional 20 min at 45 °C and 1200 rpm to alkylate newly reduced thiols.

At this stage samples were either processed immediately or stored at-20 °C until further use.

Prior to proteolytic digestion, samples were briefly centrifuged; frozen samples were thawed at room temperature if necessary. 20 µg of MassSpec Grade Trypsin/Lys-C mix (Promega GmbH) were reconstituted in 200 µL resuspension buffer (Promega GmbH, composition in Table 4) on ice. Immediately, 10 µL of the freshly prepared enzyme solution (0.1 µg· μL^{-1}) or a thawed aliquot were added to each sample, resulting in an enzyme-to-protein ratio of 1:20. Samples were vortexed and digested overnight at 37 °C and 1200 rpm for 16 h on a thermoshaker.

Table 4: Composition of Trypsin/Lys C resuspension buffer.

Compound	Concentration [mM]
Acetic acid	0.05% (v/v)
$CaCl_2$	2 mM
Water	-

3.4.4 SDB-RPS peptide desalting

Following digestion and a brief centrifugation step, samples were partially dried in a vacuum concentrator (SpeedVac) at 45 °C for 30 - 40 min to reduce sample volume to approximately 30 µL. Peptide desalting was performed using StageTips packed with polystyrenedivinylbenzene reversed-phase sulfonate material (SDB-RPS; Empore™ 2241, 12 µm particle size, 47 mm; CDS Analytical LLC).

StageTips were prepared by carefully compressing three layers of SDB-RPS material into 200 µL pipette tips and placing them into 2 mL waste tube using centrifuge adapters. After labeling, StageTips were conditioned by adding 100 µL SDB-RPS loading buffer 1 (Table 5) and centrifuged for 5 min at 1000 g.

Samples were reconstituted in 120 µL of SDB-RPS loading buffer 1 by repeated up and down pipetting and transferred onto the conditioned StageTips.

To minimize sample loss, sample tubes were rinsed with an additional 40 µL of loading buffer 1. Samples were loaded by centrifugation for 7 min at 1200 g allowing the entire solution to pass through the RPS material. The flow-through was discarded before washing the StageTips with 100 µL of loading/wash buffer 1, followed by centrifugation for 5 min at 1500 g.

Subsequently, 100 µL of wash buffer 2 (Table 5) were added to the StageTips and centrifuged under the same conditions. StageTips, including adapters, were then transferred to storage tubes containing LC-MS glass inlets. Peptides were eluted by adding 60 µL SDB-RPS elution buffer (Table 6) and centrifuging for 8 min at 1500 g.

Eluted peptides were dried in a vacuum concentrator at 45 °C and stored at -20 °C until further processing.

Table 5: Composition of SDB-RPS loading and wash buffer 1 and wash buffer 2.

	Compound	Formulation % (v/v)
Loading and wash buffer 1	Isopropanol	99
	Trifluoroacetic acid 99%	1
Wash buffer 2	Water	94.8
	Acetonitrile 100%	5
	Trifluoroacetic acid 99%	0.2

Table 6: Composition of SDB-RPS elution buffer.

Compound	Formulation % (v/v)
Acetonitrile 100%	39.8
Water	59.7
NH_4OH 28%	0.5

3.4.5 Peptide Reconstitution

For LC-MS analysis, desalted and dried redox proteome samples were reconstituted in 5 µL formic acid (30% (v/v)) containing synthetic standard peptides at 10 fmol and subsequently diluted with 40 µL MS loading buffer (Table 7) by repeated up and down pipetting. Subsequently, 400 µL of water were placed in the storage tubes and the glass inlets were reinserted.

Samples were sonicated in an ultrasonic bath for 5 min at room temperature and 40% power. To ensure complete sample recovery at the bottom of the glass inlets, tubes were centrifuged for 7 min at 5000 g. Glass inlets were transferred into labeled glass vials for LC-MS measurement.

Table 7: Composition of MS loading buffer.

Compound	Formulation % (v/v)
Water	97.7
Acetonitrile 100%	2
Trifluoroacetic acid 99%	0.3

3.4.6 Nano liquid chromatography and mass spectrometer instrument parameters

Chromatographic separation was carried out using a Dionex UltiMate™ 3000 RSLCnano system (Thermo Fisher Scientific). A 5 µL aliquot of the reconstituted sample was initially loaded onto a precolumn (Acclaim™ PepMap™ C18 100, Thermo Fisher Scientific) utilizing solvent A (99.9% water, 0.1% formic acid) at a flow rate of 10 $\mu L \cdot min^{-1}$. Subsequently, peptides were eluted from the precolumn onto the analytical column (Aurora series emitter column, 1.6 µm C18, 25 cm × 75 µm, IonOpticks) using a gradient from 12% to 42% solvent B (79.9% acetonitrile, 20% water, 0.1% formic acid) over 90 min, with a flow rate of 300 $nL \cdot min^{-1}$. The total chromatographic run time, including equilibration and column washing steps, was 140 min.

Mass spectrometric analysis was conducted on a timsTOF Pro mass spectrometer (Bruker Daltonics) operating in parallel accumulation-serial fragmentation (PASEF) and data-dependent acquisition (DDA) mode. MS1 and MS2 spectra were acquired across an m/z range of 100 to 1700. Ion mobility separation was achieved using an inverse reduced ion mobility ($1/K_0$) scan range of 0.6 to 1.6 $Vs \cdot cm^{-2}$, with a total ramp time of 100 ms. Each acquisition cycle consisted of 10 PASEF MS/MS scans, resulting in a total cycle time of 1.16 s.

3.5 Data processing and statistical analysis

Raw mass spectrometry data were processed using MaxQuant software (version 1.6.17.0) with the integrated Andromeda search engine. Protein identification and label-free quantification (LFQ) were performed against a non-redundant UniProt human FASTA database. The false discovery rate (FDR) was set to 0.01 at both the peptide-spectrum match (PSM) and protein levels, allowing for up to two missed cleavages per peptide. The “match between runs” feature was enabled with a matching time window of 0.7 min and an alignment window of 20 min. MS/MS mass tolerance was set to 40 ppm, and at least one unique peptide was required for protein identification.

Two separate database searches were performed. In the classic search, carbamidomethylation of cysteine was specified as a fixed modification, while methionine oxidation and N-terminal acetylation were set as dynamic modifications. In the NEM/d5-NEM search, carbamidomethylation was omitted and NEM as well as d5-NEM modifications were defined as variable, alongside methionine oxidation and N-terminal acetylation.

Data processing was carried out in Perseus (version 1.6.14.0). Proteins identified only by site, reverse sequences, and common contaminants were removed from the cell-based datasets. LFQ intensities were $\log_2$-transformed, and proteins were retained only if they were identified in at least 70% of samples within a given experimental group (corresponding to at least three out of four biological replicates).

For preliminary protein mix experiments, filtering criteria were adapted to account for the limited number of proteins. Proteins were kept if identified in at least two of three replicates, and contaminant filtering was not applied, as albumin - part of the defined protein mixture - is typically flagged as a contaminant.

Processed data were exported to Microsoft Excel for determination of sequence coverage, peptide counts, mean LFQ intensities, and modification frequencies. Amino acid sequences of ubiquitin, albumin, cytochrome c and thioredoxin reductase 1 were retrieved from UniProt database to identify cysteine residues, including free thiols and residues involved in disulfide bonds.

For cell proteome profiling, principal component analysis (PCA) and volcano plots were generated in Perseus. Missing values were imputed from a Gaussian distribution, and statistical significance was assessed by two-sided t-tests with $s_0 = 0.1$ and FDR = 0.05.

For extended analyses and data visualization, processed datasets were imported into Python 3 and GraphPad Prism (version 8.0.1). Python-based analyses utilized the packages pandas, numpy, matplotlib, and seaborn. General data handling and additional calculations were performed in Microsoft Excel.

Protein-protein interaction networks were generated using STRING database analysis (string-db.org) for selected sets of significantly regulated proteins. Venn diagrams were generated using Venny 2.1 to identify overlaps between protein or modification sets. Final visualizations were created in Python.

4 Results and Discussion

4.1 MTT cytotoxic assays

MTT cytotoxicity assays were performed to determine the half-maximal inhibitory concentration (IC_{50}) of TBHP and to identify suitable treatment concentrations for inducing different levels of oxidative stress. The MTT assay assesses cell viability based on the metabolic reduction of the tetrazolium salt MTT (3-(4,5-dimethylthiazol-2-yl)-2,5-diphenyltetrazolium bromide) to insoluble purple formazan by NAD(P)H-dependent oxidoreductase enzymes in metabolically active cells.[47] Consequently, the measured absorbance directly reflects cellular metabolic activity and viability.

Dose-response curves for Detroit 551 fibroblasts and SW480 colon carcinoma cells following TBHP treatment are shown in Figure 7. All assays were performed with both biological and technical replicates. For Detroit 551 cells, two independent researchers conducted six technical replicates each. For SW480 cells, experiments were performed on two separate days by two researchers, yielding in a total of 15 technical replicates. Data are presented as mean ± standard deviation (SD).

The IC_{50} of TBHP was determined to be 63 ± 2 µM in Detroit 551 cells and 45 ± 3 µM in SW480 cells. Based on these results, TBHP concentrations of 16 µM and 63 µM were selected for SW480 cells to represent sub-lethal and enhanced stress conditions, respectively. Although this concentration exceeded the IC_{50} value, cells remained adherent after 24 h of treatment, indicating metabolic inactivation rather than immediate cell loss. In Detroit 551 fibroblasts, a TBHP concentration close to the IC_{50} (60 µM) was selected for subsequent experiments.

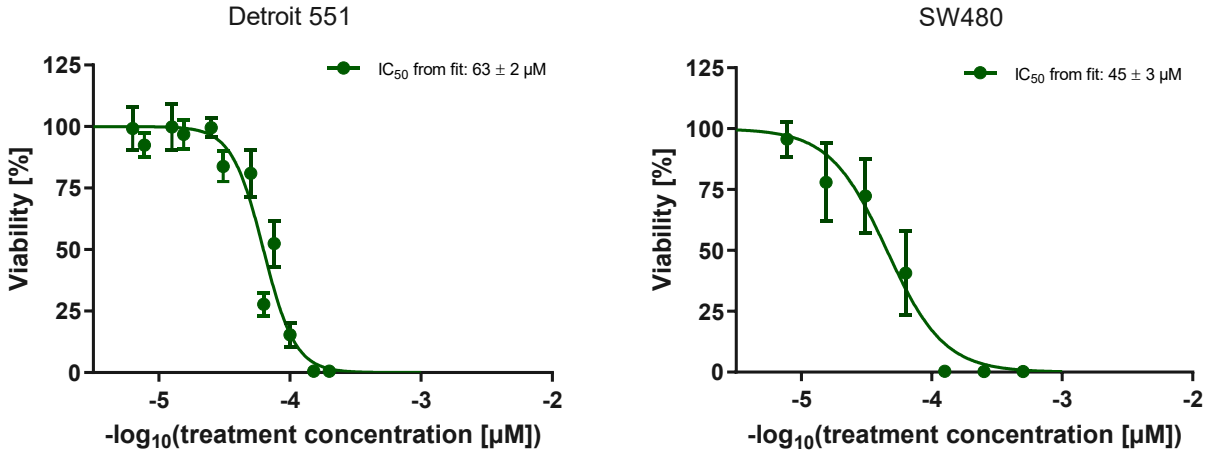

Figure 7: Results of the MTT cytotoxic assays following TBHP treatment. Dose-response curves for Detroit 551 fibroblasts (right) and SW480 colon carcinoma cells (left). Cell viability is shown as a function of TBHP concentration. Data are presented as mean ± SD. IC_{50} values were determined by nonlinear regression analysis.

The higher IC_{50} observed in Detroit 551 cells is consistent with an increased resistance of fibroblasts to oxidative stress compared to cancer cells, potentially reflecting more effective antioxidant buffering capacity and a lower basal ROS level relative to SW480 cells due to slower proliferation.[48,49]

For ATO, a treatment concentration of 5 µM was selected, as this dose has previously been established within the research group as sufficient to induce oxidative stress and DNA damage in SW480 cells.[42] Additional MTT cytotoxicity assays with ATO were performed to validate the suitability of this concentration under the experimental conditions used in this study.

During the MTT cytotoxicity assays, a relevant technical observation was made when TBHP-treated and ATO-treated SW480 samples were incubated on the same microtiter plate. As shown in **Figure 8**, wells corresponding to TBHP treatment (rows 4-6) exhibited pronounced vapor-related effects after the 4 h MTT incubation period. These effects extended to neighboring wells containing ATO-treated cells (rows 1-3), as indicated by altered formazan staining intensity.

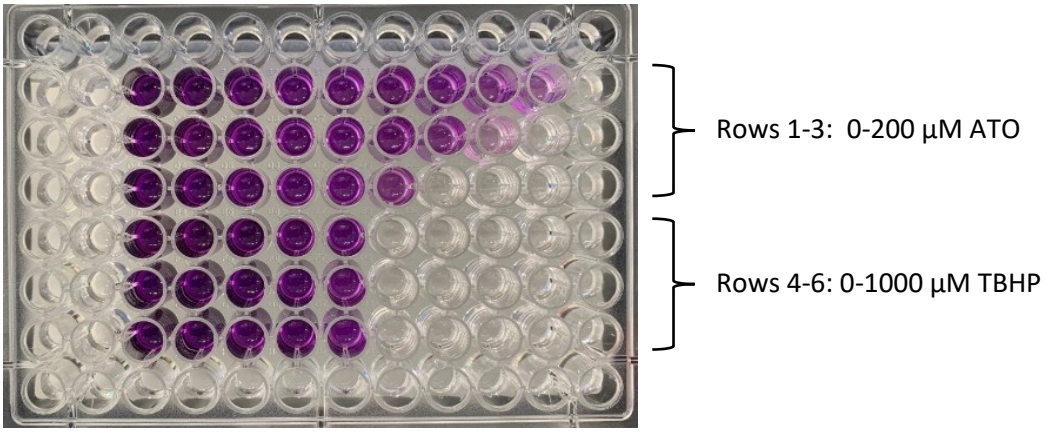

Figure 8: Representative image of an MTT assay plate illustrating vapor-related cross-contamination during TBHP treatment in SW480 cells. Wells in rows 4-6 contained TBHP-treated samples, while wells in rows 1-3 contained ATO-treated samples. Altered formazan staining intensity in ATO-treated wells indicates unintended exposure to TBHP vapor during incubation.

This observation is attributed to the relatively low boiling point of TBHP (approximately 35 °C), which is below the incubation temperature used for the assay (37 °C). Partial evaporation of TBHP during incubation likely resulted in vapor-phase diffusion to neighboring wells within the plate, leading to unintended exposure of adjacent wells and thereby influencing the apparent MTT readout of the ATO-treated samples.

To prevent this cross-contamination effect, TBHP treatments were subsequently performed on separate microtiter plates in all further experiments.

4.2 Development of a method to assess protein redox status in cell-free mixtures

As an initial pre-experiment, a 20 µg protein mixture consisting of ubiquitin (Ubi, bovine), cytochrome c (CytC, equine), albumin (Alb, human), and thioredoxin reductase 1 (TXNRD1, human) was prepared to evaluate the performance of the redox-specific digestion and labeling workflow prior to its application to complex cell lysates. The selected proteins (each 5 µg) represent a broad spectrum of cysteine-related chemistries and redox states.

Ubiquitin lacks cysteine residues and therefore served as a negative control for thiol-specific labeling. Cytochrome c contains two intramolecular disulfide bonds. Albumin comprises 35 cysteine residues, including 17 disulfide bonds and one free thiol group. TXNRD1 is a selenoprotein harbouring a Cys-Sec motif that forms a selenylsulfide bond (-SeS-), in addition to cysteine residues in reduced or oxidized states. This protein panel (summarized in Table 8) therefore provided a suitable test system to assess modification efficiency, specificity, and detectability of different redox states by differential alkylation.

Table 8: Number of cysteines and selenocysteine residues, including thiol groups (-SH), disulfide bonds (-SS-) and selenylsulfide bonds (-SeS-), in the proteins used for the pre-experiment. Information was retrieved from UniProt.

Protein	N° Cys/Se	N° -SH	N° -SS-	N° -SeS-
Ubiquitin (bovine)	0	0	0	0
Cytochrome C (equine)	2	0	2	0
Albumin (human)	35	1	17	0
Thioredoxin reductase 1 (human)	17	9	2	1

4.2.1 Comparison of classic and NEM/d5-NEM database search strategies

Sequence coverage and peptide identification results obtained from classic and NEM/d5-NEM database searches are summarized in Figure 9 and Tables 9 and 10. In the classic search, carbamidomethylation of cysteine residues was specified as a fixed modification, assuming all cysteines to be alkylated and that no redox-specific information is retained. In contrast, the NEM/d5-NEM search omitted carbamidomethylation and included NEM and isotopically labeled d5-NEM as variable cysteine modifications. This configuration reflects the applied differential alkylation workflow and enables discrimination between initially reduced and reversibly oxidized cysteine residues at the peptide level.

As expected, ubiquitin exhibited nearly identical sequence coverage (97.2%) and peptide counts in both searches, consistent with the absence of cysteine residues in its sequence.

Cytochrome c showed a moderate increase in sequence coverage from 61.0% in the classic database search to 69.5% when analyzed using the NEM/d5-NEM search parameters, accompanied by an increase in peptide identifications. Although overall coverage remained comparatively low - likely due to limited proteolytic accessibility associated with its compact tertiary structure and bound heme-group of cytochrome c [50] - the NEM/d5-NEM search yielded a measurable increase in sequence coverage and identifiable peptides compared to the classic search.

The most pronounced differences between database search strategies were observed for albumin and TXNRD1. Allowing NEM and d5-NEM as variable modifications enabled detection of modified peptides that were excluded in the classic search, resulting in substantial increases in sequence coverage and peptide identifications. Albumin sequence coverage increased from 55.8% to 93.8%, and TXNRD1 coverage from 69.3% to 98.2%, accompanied by marked increases in peptide counts. These results demonstrate that inclusion of NEM and d5-NEM as variable modifications substantially improves identification of cysteine-rich proteins and supports the technical applicability of the workflow for subsequent redox-focused experiments.

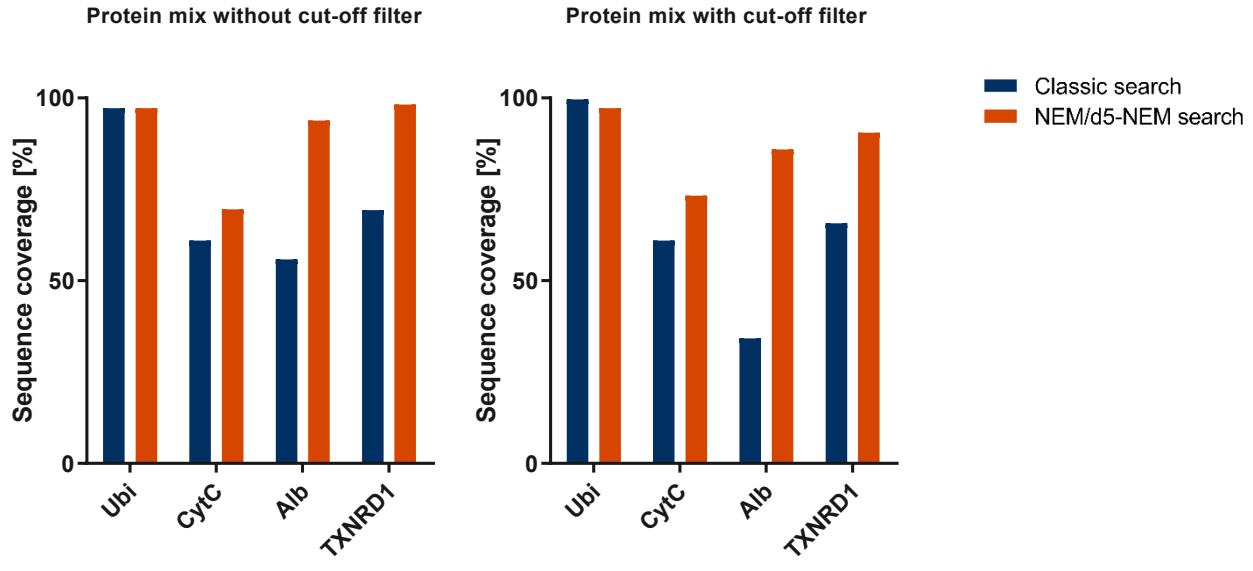

Figure 9: Sequence coverage in the classic and NEM/d5-NEM database searches for the protein mixture experiments. Results from the first experiment without cut-off filters (left) and the second experiment with cut-off filter implementation (right) are shown.

Table 9: Sequence coverage (%) of ubiquitin, cytochrome c, albumin and thioredoxin reductase 1 obtained from the classic and NEM/d5-NEM database searches for protein mix experiments, with and without implementation of molecular weight cut-off filters

Sequence coverage [%]	Protein mix without cut-off filter		Protein mix with cut-off filter	
	Classic search	NEM/d5-NEM search	Classic search	NEM/d5-NEM search
Ubiquitin	97.2	97.2	99.6	97.2
Cytochrome c	61.0	69.5	61.0	73.3
Albumin	55.8	93.8	34.2	85.9
Thioredoxin reductase 1	69.3	98.2	65.7	90.5

Table 10: Comparison of peptide identifications in the classic and NEM/d5-NEM database searches, with and without the implementation of cut-off filters.

N° peptides	Protein mix without cut-off filter		Protein mix with cut-off filter	
	Classic search	NEM/d5-NEM search	Classic search	NEM/d5-NEM search
Ubiquitin	20	21	19	19
Cytochrome c	19	23	19	23
Albumin	61	242	31	104
Thioredoxin reductase 1	98	153	52	72

4.2.2 Evaluation and optimization of the differential alkylation workflow

Analysis of peptide-level modification patterns in the initial protein mixture experiment revealed substantial heterogeneity, with multiple modification variants frequently detected for the same cysteine residue and no single modification state predominating. A pronounced bias toward NEM-modified cysteines was observed, indicating an overrepresentation of reduced thiol labeling (Figure 10). This heterogeneity hindered unambiguous assignment of cysteine redox states.

The observed bias was attributed to residual NEM present during the TCEP-mediated reduction step. As TCEP reduces disulfide bonds more rapidly than it reacts with free NEM,[35,51] newly reduced thiols could still be alkylated by residual NEM present in the sample,[46] introducing modification patterns that do not reflect the original redox state of the sample, but a sample preparation artefact.

To address this issue, molecular weight cut-off filters were incorporated into the workflow to remove excess NEM prior to reduction via TCEP. While implementation of the cut-off filters resulted in a reduced total number of identified peptides for ubiquitin, albumin, and TXNRD1, overall protein sequence coverage remained high (Table 10). For example, albumin sequence coverage decreased from 93.8% to 85.9% and TXNRD1 from 98.2% to 90.5% in the NEM/d5-NEM search, indicating that overall protein coverage was largely preserved (Table 9).

Quantitative comparison of thiol modification patterns demonstrated a clear improvement in peptide-level resolution following implementation of the cut-off filter during sample preparation to remove residual NEM. Normalized LFQ intensity distributions showed broadly dispersed modification states in the absence of filtering, whereas incorporation of the cut-off step resulted in consolidation toward predominantly NEM- or d5-NEM-labeled species for individual peptides. This effect was particularly pronounced for albumin and TXNRD1 peptides, including albumin peptides *QNCELFEQLGEYK* and *AAFTECCQAADK*, and TXNRD1 peptide *WGLGGTCVNVGCIPKK*. According to UniProt annotation, the cysteines within these peptides are physiologically engaged in disulfide bonds. Consequently, the observed shift toward predominantly d5-NEM labeling yielded modification patterns more consistent with the expected redox states (Figure 10).

In contrast, the TXNRD1 peptide *VVAQSTNSEEIIEGEYNTVMLAIGRDACTR*, containing a cysteine not annotated as forming a disulfide in UniProt, was detected exclusively as NEM-modified in both workflows, demonstrating that the optimized workflow preserves efficient capture of free thiols.

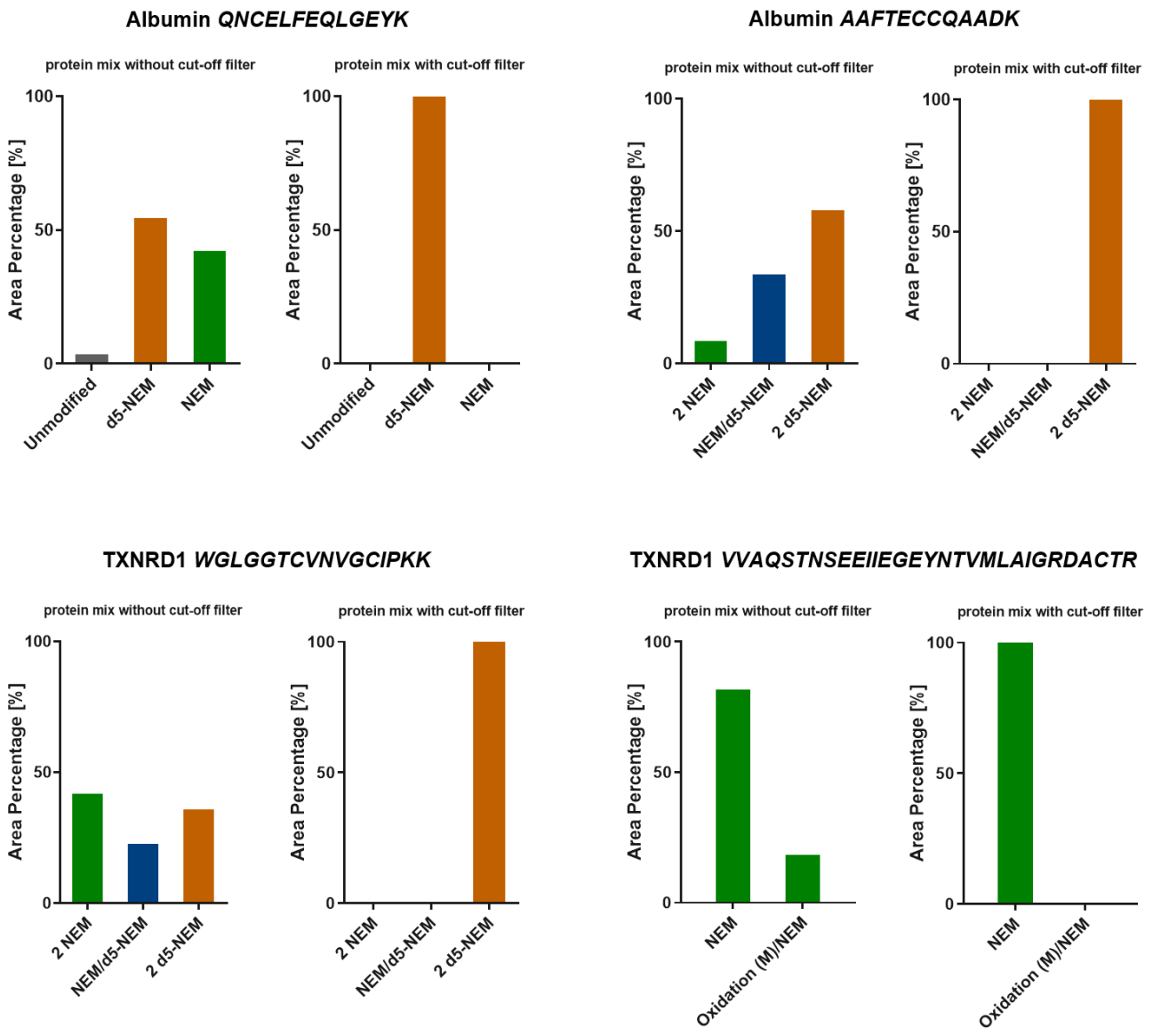

Figure 10: LFQ intensity-based quantification of differentially alkylated peptide variants illustrating the effect of cut-off filter implementation in the protein mix experiment. Mean normalized LFQ intensities are shown for human serum albumin peptides *QNCELFEQLGYK* and *AAFTECCQAADK*, and the TXNRD1 peptide *WGLGGTCVNVGCIPKK* and *VVAQSTNSEEIIEGEYNTVMLAIGRDACTR*. The plots compare results obtained without and with the cut-off filter step. The shown albumin peptides and the TXNRD1 *WGLGGTCVNVGCIPKK* contain cysteines annotated as disulfide bonds under physiological conditions, whereas the cysteine in the TXNRD1 peptide *VVAQSTNSEEIIEGEYNTVMLAIGRDACTR* is not assigned to a disulfide bond according to UniProt.

4.3 Cell experiments: PCA and volcano plot analysis

For the cell-based redox proteomics experiments, SW480 colon carcinoma cells and Detroit 551 fibroblasts were treated with defined oxidative and inflammatory stimuli. SW480 cells were exposed for 24 h to TBHP at 16 µM and 63 µM, or ATO at 5 µM. Detroit 551 cells were treated with 60 µM TBHP and/or 10 ng·mL^{-1} IL-1β for a total incubation time of 4 h. All experimental conditions were performed in four biological replicates and analyzed by LC-MS/MS following differential alkylation using NEM and d5-NEM.

Principal component analysis (PCA) was performed to assess global variation and sample clustering in the SW480 and Detroit 551 cell-based redox proteomics datasets.

PCA of the Detroit 551 dataset showed pronounced dispersion of samples, particularly among control replicates (**Figure 11**). This extensive variability substantially reduced the statistical power to detect treatment-associated effects, and no reliable clustering of treatment groups was observed. The origin of this variability likely occurred at an early experimental stage, most plausibly during cell lysis. Consistent with this interpretation, BCA protein quantification revealed substantial variation in protein concentrations between conditions and biological replicates. One plausible explanation is partial cell loss during PBS washing steps prior to lysis, potentially due to weaker adhesion of Detroit 551 fibroblasts to the 6-well plate surface, resulting in inconsistent protein recovery.

Due to the pronounced technical variability and lack of reproducible separation between treatment groups, the Detroit 551 dataset was excluded from further analysis.

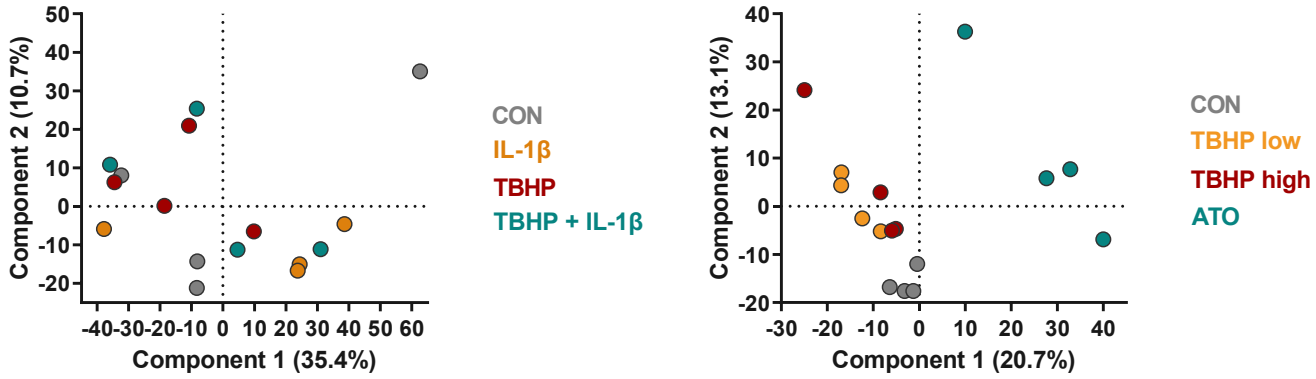

Figure 11: Principal component analysis (PCA) of proteomic data from (left) Detroit 551 cells treated with control (CON), IL-1β (10 ng·mL^{-1}), TBHP (60 µM) or TBHP + IL-1β, and (right) SW480 cells treated with control (CON), TBHP at 16 µM (low) or 63 µM (high) or ATO (5 µM). Each point represents an individual biological replicate.

In SW480 cells, PCA revealed a clear separation of treatment conditions, demonstrating consistent proteomic responses to TBHP and ATO across biological replicates (**Figure 11**). Notably, samples treated with ATO showed a stronger separation from control conditions than TBHP-treated samples, whereas no distinct separation was observed between the lower (16 µM) and higher (63 µM) TBHP concentrations.

Volcano plots were generated from the NEM/d5-NEM database search to assess treatment-induced changes in protein abundance in SW480 cells (**Figure 12**). ATO treatment resulted in pronounced protein regulation, with 627 proteins significantly altered compared to control conditions, including 258 upregulated and 369 downregulated proteins. In contrast, TBHP treatment at both low (16 µM) and high (63 µM) level did not result in the expected degree of significant protein regulation, as only few or no proteins passed the applied significance thresholds. Specifically, no significantly regulated proteins were detected following treatment with 16 µM TBHP, whereas only three significantly upregulated proteins were identified at 63 µM TBHP.

Consequently, subsequent analyses focused on the ATO-treated dataset. TBHP-treated samples were not further considered for protein abundance analysis but were retained for redox-specific evaluation, as changes in cysteine redox states are not necessarily coupled to significant protein regulation.

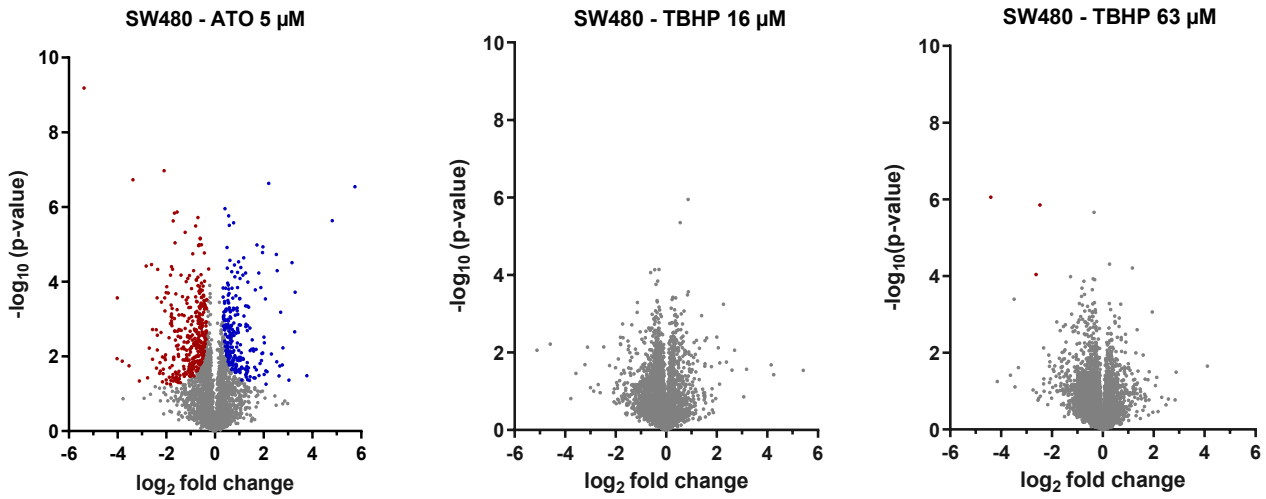

Figure 12: Volcano plots illustrating differential protein regulation in SW480 cells following treatment with 5 µM ATO (left), 16 µM TBHP (middle) and 63 µM TBHP (right) based on the NEM/d5-NEM database search. Red dots represent significantly down-regulated proteins, while blue ones show significantly up-regulated proteins. Grey dots indicate not significantly regulated proteins.

4.4 ATO - mode of action in SW480 cells

ATO is known to affect cancer cells through activation of diverse signaling pathways and modulation of multiple cellular functions. Besides degradation of the oncoprotein PML-RARα in acute promyelocytic leukaemia (APL) cells, ATO treatment additionally induces reactive oxygen species, heat shock protein expression, kinase signaling, cell-cycle disruption and apoptosis in on APL-cells.[42]

Interpretation of the proteomic regulation in this experiment was informed by a published ATO (phospho)-proteomics study by Bortel et al., which served as a reference framework for expected cellular responses.[42]

To support the biological interpretation of the regulated proteins, a STRING protein-protein interaction network analysis was performed using a selected subset of 27 significantly regulated proteins relevant to the established mode of action of ATO (**Figure 13**).

Activation of oxidative stress and NRF2 signaling

The NRF2 pathway represents a key cellular defense system controlling the expression of antioxidant and protective genes during oxidative stress.[52] The most strongly upregulated protein was HMOX1, a well-established NRF2 target and classical marker of oxidative stress. HMOX1 degrades heme and contributes to tumor-suppressive processes.[53]

Upregulation of additional NRF2-regulated proteins, including SRXN1, GCLM, TXNRD1, SQSTM1 and the ferritin light chain FTL, further supports activation of the NRF2-mediated antioxidant response.[42]

Functionally, SRXN1 restores oxidized peroxiredoxins, GCLM promotes glutathione biosynthesis, and TXNRD1 reduces thioredoxin, together supporting detoxification of reactive oxygen species.[54,55] SQSTM1 links oxidative stress responses with autophagy and activates NRF2 via KEAP1 binding, thereby reinforcing antioxidant gene expression.[56] FTL stores intracellular iron, limiting iron-driven oxidative damage.[57]

Proteostasis and heat shock response

Multiple heat shock proteins were strongly upregulated, predominantly members of the HSP70 family (HSPA1A, HSPA6, HSPA8, HSPA4, HSPA4L) as well as the HSP110 family member HSPH1 and the chaperonin TCP1.

Heat shock proteins function as molecular chaperones that stabilize unfolded proteins, refold damaged proteins and prevent protein aggregation during cellular stress.[58] Their coordinated upregulation indicates enhanced protein quality control activity.

Apoptosis and cell-cycle disruption

ATO treatment increased the abundance of NDRG1, a protein involved in p53-dependent apoptotic signaling, which is a common response pathway in cancer therapy.[59]

In addition, upregulation of tumor necrosis factor receptors TNFRSF10B and TNFRSF10D points toward modulation of death-receptor apoptotic pathways, which are established contributors to ATO-induced cell death.[42]

Dysregulation of CCNB1 may further sensitize cells to apoptosis by promoting stress-associated cell-cycle arrest.[60]

Kinase signaling

Components of MAPK/AP-1 signaling were affected, as indicated by the upregulation of FOSL1, FOSL2, and SPAG9. MAPK signaling transmits stress signals through phosphorylation and regulates transcription factors such as AP-1, a complex composed of FOS and JUN family members, thereby activating kinase-dependent transcriptional programs.[42,61]

In addition, the casein kinase family members CSNK1A1 and CSNK2A2 were upregulated. Although phosphorylation events were not assessed in this study, altered abundance of these kinases suggests modulation of kinase-associated signaling processes in response to ATO.[42]

Suppression of redox, transcriptional, and DNA repair pathways

In contrast to stress-induced pathways, several proteins involved in redox regulation, transcriptional control and genome integrity were downregulated upon ATO exposure.

TXNL1, a thioredoxin-like protein and the most strongly downregulated protein in this dataset, reflects a reduced capacity to maintain protein thiol redox balance and protect cells from oxidative damage.[62]

The transcription factor SP1 and the DNA methyltransferase DNMT1 were significantly reduced, indicating altered transcriptional regulation and disruption of epigenetic stability. SP1 regulates expression of numerous genes involved in cell growth and survival, while DNMT1 maintains DNA methylation patterns during replication.[63,64]

Furthermore, decreased levels of the DNA repair proteins MSH2 and FANCD2 are related to impairment of DNA damage response pathways.[65]

Overall, the observed proteomic profile demonstrates that ATO induces a multifaceted stress response characterized by activation of antioxidant defenses, proteostasis mechanisms, kinase signaling, and apoptotic pathways, while simultaneously suppressing DNA repair capacity and epigenetic maintenance.

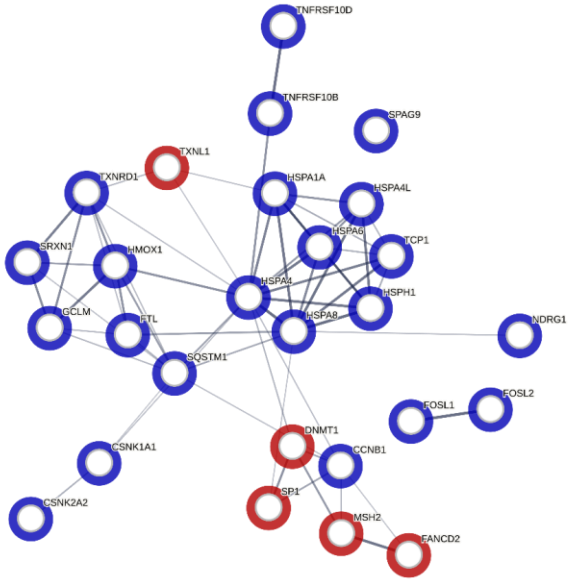

Figure 13: STRING protein-protein interaction network of selected proteins significantly regulated upon ATO treatment in SW480 cells (significantly up- or downregulated in at least three out of four biological replicates). Proteins were selected based on their relevance to established ATO-associated pathways as described by Bortel et al.[42] Nodes represent individual proteins, with blue indicating upregulated and red indicating downregulated proteins. Edges indicate known or predicted functional associations, and edge thickness reflects interaction confidence based on STRING evidence scores.

4.5 Redox proteomic profiling based in cysteine modifications *in vitro*

To evaluate the efficiency of the differential alkylation workflow, the extent of NEM/d5-NEM modification was assessed in the SW480 dataset. Modification entries were first filtered to include only those detected in at least three out of four biological replicates. Subsequently, only modifications assigned to cysteine-containing peptides were retained. At this stage, the dataset still contained various modification types, such as unmodified peptides, methionine oxidation, and N-acetylation. Therefore, filtering criteria were further restricted to NEM and d5-NEM modifications.

Application of the replicate-based filtering strategy resulted in a consistent set of approximately 17,000 - 18,000 robust modification entries per condition, of which roughly 2,100 - 2,300 were localized to cysteine-containing peptides. More than 99% of these cysteine-associated modifications corresponded to either NEM or d5-NEM across all treatment conditions, resulting in an overall modification extent ranging from 99.4% to 99.7% (**Table 11**).

This analysis includes sequence duplicates and therefore does not represent unique cysteine sites but rather provides a measure of the overall efficiency of cysteine alkylation achieved by the applied workflow.

The consistently high modification extent across all conditions demonstrates efficient cysteine alkylation among detected peptides and indicates that alkylation efficiency was not comprised by TBHP or ATO treatment. These results provide a robust foundation for subsequent redox-specific analyses.

Table 11: Extent of NEM/d5-NEM modification in the SW480 dataset following filtering criteria.

	CON	TBHP low	TBHP high	ATO
N° Modifications	18 327	17 605	17 707	17 280
N° Modifications on C-peptides	2 322	2 102	2 131	2 127
N° NEM/d5-NEM modifications on C-peptides	2 311	2 095	2 121	2 114
Extent of NEM/d5-NEM modification	**99.5%**	**99.7%**	**99.5%**	**99.4%**

4.5.1 Distribution of NEM and d5-NEM cysteine modifications

The relative distribution of NEM, d5-NEM, and mixed NEM/d5-NEM modifications on cysteine residues was evaluated for each experimental condition (**Figure 14**). Based on the experimental design, an increased proportion of d5-NEM modifications was expected under stress conditions, reflecting oxidation events.

However, the relative proportions of NEM-, d5-NEM-, and mixed-labeled cysteine residues were highly similar across all treatment conditions. In all samples, NEM modifications constituted the largest fraction, followed by d5-NEM modifications, while mixed NEM/d5-NEM states represented only a minor proportion. Neither TBHP nor ATO treatment resulted in a pronounced global shift toward increased d5-NEM labeling compared to the control samples. Thus, at the level of modification entries, including sequence duplicates, no clear global differences in cysteine oxidation could be detected between control and oxidative stress conditions.

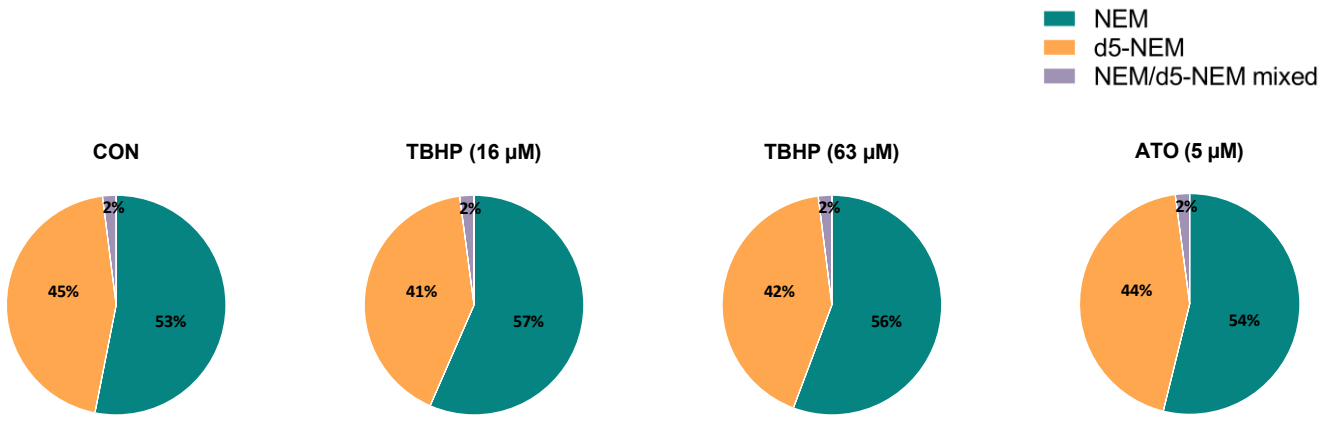

Figure 14: Relative distribution of NEM-, d5-NEM-, and mixed NEM/d5-NEM-modified cysteine-containing peptides across control (CON), low TBHP (16 µM), high TBHP (63 µM) and ATO (5 µM) treatment conditions in the SW480 dataset. Modification patterns were highly similar across all conditions, indicating no pronounced global shift toward increased cysteine oxidation under the applied oxidative stress conditions. NEM-modified peptides constituted the largest fraction, followed by d5-NEM-modified peptides, while mixed labeling represented only a minor proportion (2%).

4.5.2 Extent of NEM/d5-NEM modified cysteine peptides across proteins

To assess the distribution of cysteine-modified peptides across proteins, the analysis was performed aft er removal of peptide sequence duplicates. Only peptides detected in at least three out of four biological replicates were retained. Protein identifiers were extracted from the filtered peptide list, and duplicate protein entries were removed to obtain a non-redundant protein dataset.

As summarized in **Table 12**, this filtering strategy resulted in 1,417 - 1,554 unique cysteine-containing peptide sequences per condition, corresponding to 753 - 822 non-redundant proteins across the treatment groups. Comparable numbers of cysteine-modified peptides and proteins were observed for control, TBHP-treated, and ATO-treated samples, indicating a consistent proteome-wide distribution of detectable cysteine modifications under all experimental conditions.

These values are in good agreement with previously published redox proteomics studies, employing comparable differential alkylation workflows. For example, the group of Birner-Gruenberger reported detection of 1,834 cysteine-containing peptide features across 921 proteins,[45] which formed the methodological basis for the workflow in this study. In a subsequent study they reported quantification of more than 1,900 cysteine residues across approximately 900 - 950 proteins following workflow optimization.[46] The comparable scale of cysteine and protein coverage achieved in the present dataset supports the robustness and successful implementation of the applied redox proteomics approach. Consistent with this overall robustness, no relevant differences in peptide or protein coverage were observed between control, TBHP-treated, and ATO-treated samples, indicating that oxidative stress conditions did not compromise alkylation efficiency or peptide detectability.

Table 12: Peptide- and protein-level coverage of NEM/d5-NEM–modified cysteine residues across treatment conditions in the SW480 dataset.

	CON	TBHP low	TBHP high	ATO
N° peptides	16839	16268	16332	15892
N° C-peptides	1554	1423	1438	1417
N° NEM/d5-NEM modified C-peptides	**1547**	**1418**	**1434**	**1412**
N° proteins	**822**	**753**	**772**	**771**

4.5.3 Treatment-specific differences in unique cysteine modified peptides

Up to this stage, the global metrics of cysteine modification - including the number of cysteine-containing peptides and the number of proteins harboring cysteine modifications - were highly comparable across all experimental conditions. This indicated that treatment-induced redox effects were not reflected at the global level of cysteine

modification. However, such global analyses may mask condition-specific effects that emerge only at peptide-resolved resolution.

To address this, the analysis was refined by focusing on unique peptide-protein identifiers, generated by combining peptide sequences with their corresponding UniProt accession numbers. For simplicity, these entries are referred to as *unique peptides* in the following analysis. Unique peptides modified by either NEM or d5-NEM were then compared between control and ATO conditions using Venn diagrams (Figure 15).

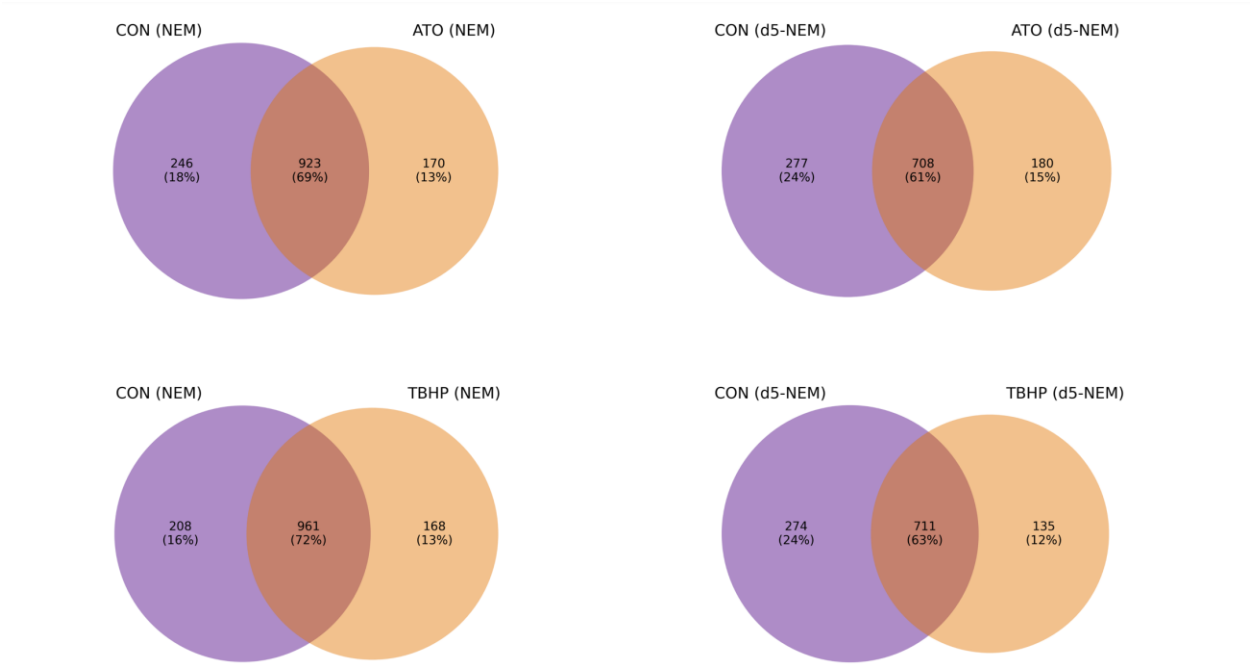

Figure 15: Venn diagram comparison of unique peptides carrying NEM (left panels) and d5-NEM (right panels) modifications between control and ATO-treated (top panels) or TBHP-treated (bottom panels) SW480 cells. Numbers indicate shared and condition-specific unique peptides, illustrating treatment-dependent differences in cysteine modification patterns. Mixed NEM/d5-NEM modifications were excluded from this analysis.

Despite substantial overlap between conditions, clear treatment-specific differences were observed at the level of individual cysteine-modified peptides. For ATO treatment, 69% of NEM-modified peptides were shared with the control condition, while 18% were detected exclusively in control samples and 13% were specific to ATO-treated cells. A similar pattern was observed for d5-NEM-modified peptides, with 61% shared between conditions, 24% control-specific peptides, and 15% unique to ATO treatment.

Comparable, though less pronounced, treatment-specific patterns were also observed following high-dose TBHP exposure. For NEM-modified peptides, 72% were shared between control and TBHP-treated samples, whereas 16% were unique to the control condition and 13% were specific to TBHP treatment.

For d5-NEM-modified peptides, 63% were common between conditions, with 24% control-specific and 12% TBHP-specific peptides detected.

Together, these results demonstrate that despite largely similar global modification levels, both ATO and TBHP treatments were associated with distinct profiles of cysteine-modified peptides that became evident only at peptide-level resolution.

4.5.4 Treatment-specific cysteine-modified peptides between ATO and TBHP

As both ATO and TBHP induce oxidative stress through distinct mechanisms, a direct comparison of treatment-specific unique peptides was performed to assess differences in cellular redox responses. While TBHP mainly acts as a direct peroxide source, ATO induces reactive oxygen species primarily through perturbation of intracellular signaling and redox-regulatory pathways rather than acting as a direct oxidant.[42,43] To capture treatment-specific redox signatures at peptide-level resolution, unique peptides were compared between high-dose TBHP- and ATO-treated samples for both NEM- and d5-NEM-modified peptides using Venn diagrams (**Figure 16**).

Across both labeling states, overlap between TBHP- and ATO-specific peptides was limited, indicating largely distinct cysteine modification patterns induced by the two treatments. For NEM-modified peptides, 25% were shared between TBHP and ATO conditions, whereas 37% were specific to TBHP treatment and 38% were uniquely detected following ATO exposure. A similar trend was observed for d5-NEM-modified peptides, with only 21% shared peptides, compared to 31% TBHP-specific and 48% ATO-specific peptides.

Overall, ATO and TBHP induced distinct cysteine modification patterns that reflect their different modes of action.

Figure 16: Venn diagram comparison of unique NEM-modified (left) and d5-NEM-modified (right) peptides between TBHP- and ATO-treated SW480 cells, illustrating treatment-specific differences in cysteine modification patterns. Mixed NEM/d5-NEM modifications were excluded from this analysis.

4.5.5 Linking ATO specific cysteine peptides to protein regulation under ATO treatment

To relate redox-specific peptide alterations to protein-level regulation under ATO treatment, ATO-specific unique peptides derived from both NEM- and d5-NEM-modified peptides were compared with significantly up- and downregulated proteins. Duplicate protein entries were removed prior to comparison.

Among significantly upregulated proteins, 8% overlapped with the ATO-specific peptide-derived protein list, whereas only 1% overlap was observed among downregulated proteins (**Figure 17**).

This shows that a subset of proteins exhibiting abundance regulation under ATO treatment also harbors ATO-specific cysteine-modified peptides, suggesting partial convergence between redox-specific and protein-level responses.

Figure 17: Venn diagram comparison of proteins derived from ATO-specific NEM- and d5-NEM modified unique peptides with significantly upregulated (left) and significantly downregulated (right) proteins under ATO treatment. Numbers indicate overlapping and condition-specific proteins after removal of duplicate protein identifiers.

To further explore functional relationships within these overlapping protein sets, STRING protein-protein interaction network analysis was performed separately for up- and down regulated proteins (**Figure 18**). The network derived from upregulated proteins revealed a highly interconnected cluster dominated by heat shock proteins and proteins involved in metabolic stress adaptation, including components of glycolysis and the pentose phosphate pathway. In contrast, the network derived from downregulated proteins was smaller and less connected interaction pattern.

Together, these results demonstrate that ATO-induced cysteine-specific peptide alterations only partially coincide with protein-level regulation, particularly within stress response and metabolic pathways, supporting a coordinated redox and proteomic response to ATO treatment.

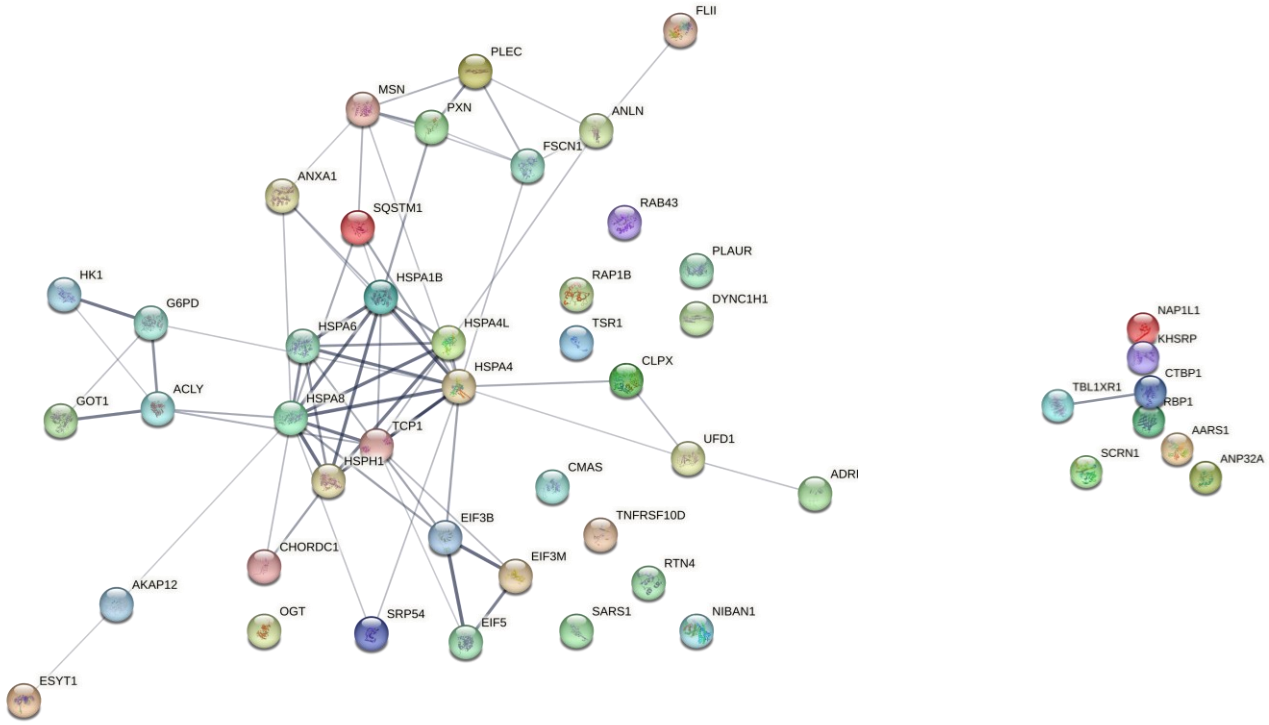

Figure 18: STRING protein-protein interaction networks of proteins overlapping between ATO-specific cysteine-modified peptides and significantly upregulated (left) or downregulated (right) proteins. Nodes represent individual proteins, and edges indicate known or predicted functional associations. Edge thickness reflects interaction confidence based on STRING evidence scores.

4.5.6 Redox-specific characterization of the heat shock protein cluster

Based on the prominent clustering of heat shock proteins (HSPs) in the STRING network, this protein group was selected for peptide-resolved redox analysis. To localize ATO-induced redox effects to specific cysteine-containing sequences, subsequent analyses were performed at the level of NEM- and d5-NEM-modified peptides. This strategy enabled site-specific assessment of cysteine redox behavior within individual HSP family members and provided the basis for functional interpretation at the residue level.

Modified cysteine residues detected in HSP family proteins were compiled to map which cysteine positions were captured by the NEM/d5-NEM workflow (**Table 13**). Proteins were grouped according to chaperone family classification based on their molecular mass including HSP60, HSP70, HSP70-related (HSP110) proteins, HSP70 co-chaperones and HSP90 family members.

Table 13: Modified cysteine residues detected in HSP family proteins. Cysteine positions are reported according to UniProt sequence.

HSP family	Modified cysteine residues
HSP60	
HSPD1	Cys237, Cys442, Cys447
HSP70	
HSPA1A	Cys17, Cys574, Cys603
HSPA6	Cys308 (homologous position to HSPA1A Cys306)
HSPA5	Cys41
HSPA8	Cys17, Cys574, Cys603
HSPA9	Cys17, Cys66, Cys608
HSP70-related (HSP 110 family)	
HSPA4	Cys167, Cys245, Cys290, Cys310, Cys367, Cys380, Cys417, Cys779
HSPA4L	Cys540
HSPH1	Cys13, Cys34, Cys140, Cys167, Cys245, Cys290, Cys310, Cys658, Cys796
HSP70 co-chaperone	
HSPBP1	Cys172, Cys214
HSP90	
HSP90AA1	Cys374, Cys420, Cys529, Cys597, Cys598
HSP90AB1	Cys366, Cys412, Cys521, Cys589, Cys590
HSP90B1	Cys645

The HSP70 superfamily plays a central role in cellular proteostasis and redox homeostasis by coordinating protein folding, refolding and degradation under stress conditions. HSP70 proteins consist of an N-terminal nucleotide-binding domain (NBD) and a C-terminal substrate-binding domain (SDB), whose activities are allosterically coupled through the ATPase cycle. ATP binding and hydrolysis in the NBD regulate substrate affinity in the SDB, thereby controlling client protein interaction and release.[58,66]

Several cysteine residues within these domains (Cys17, Cys267, Cys306, Cys574 and Cys603 in HSPA1A) have been identified as redox-sensitive regulatory sites.[58,66] Structural mapping of HSPA1A domain shows that Cys306 is located in the NBD, whereas Cys574 and Cys603 reside within the α-helical lid of the SBD,[58,67] as illustrated in Figure 19.

Cys306 has been shown to impair ATPase activity, while modification of Cys574 and Cys603 alters substrate binding and release.[58,68] In addition, HSP110 family members, which function as nucleotide exchange factors for HSP70, and other HSP70 co-chaperones further modulate HSP70 activity.[66]

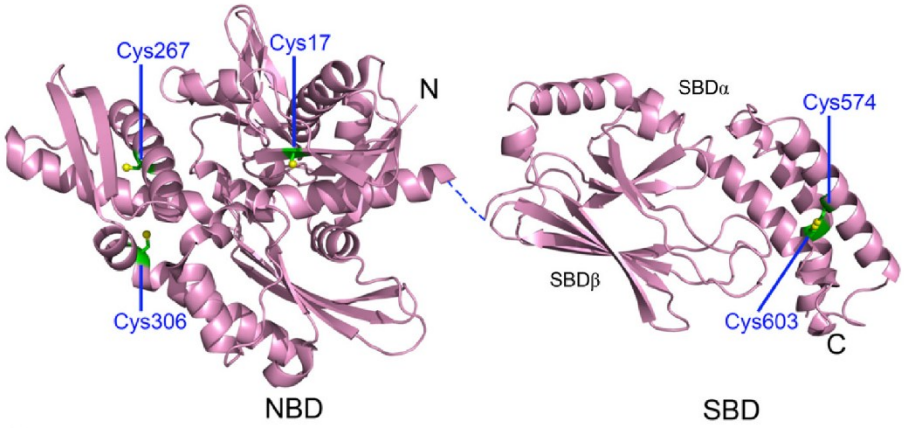

Figure 19: Structural localization of redox-sensitive cysteine residues in human HSP70 (HSPA1A). Highlighted cysteines are positioned within the nucleotide-binding domain (NBD) and substrate-binding domain (SBD). Figure adapted from Yang et al.[67]

Consistent with these reports, the present dataset detected Cys17, Cys574 and Cys603 in HSPA1A and HSPA8, as well as the homologous position Cys306 in HSPA6 (Cys308). The localization of these residues within functionally critical domains supports the conclusion that ATO-induced redox modifications preferentially target regulatory cysteine positions.

HSP90 proteins are likewise regulated by redox-sensitive cysteine residues. Cys521 has been identified as a major redox-reactive site influencing HSP90 conformation, ATPase activity and co-chaperone interactions.[66,69] In addition, the cysteine pair Cys589/Cys590 and the neighboring residues Cys597/Cys598 contribute to redox-dependent regulation of HSP90 function.[66,70] In the present study, each of these sites were detected as modified residues in HSP90AA1 and HSP90AB1, confirming their redox responsiveness under stress-inducing conditions.

Together, these findings demonstrate that cysteine modifications in HSP70 and HSP90 occur at conserved, regulatory positions controlling ATPase activity, substrate binding, and cochaperone interactions.

While the NEM/d5-NEM workflow captures cysteine residues broadly, redox modifications preferentially occur at biologically meaningful, regulatory cysteine positions rather than at random sites of oxidative damage.

Examples of peptide-level patterns

To illustrate how individual cysteine-containing HSP peptides responded to ATO treatment, selected peptides were examined in detail. In addition to the descriptive visualization shown in **Figure 20**, peptide-level statistical analyses were performed using a volcano plot derived from the modification-specific peptide dataset (**Figure 21**).

The peptide *SVVGLDVGSGSCYIAVAR* from HSPH1, containing Cys13, was detected in both NEM- and d5-NEM-modifed forms under control and ATO-treated conditions (**Figure 20**). Upon ATO exposure, both modification states increased in intensity by ~3-fold, while their relative proportions remained largely unchanged. In the peptide-level volcano analysis, this peptide was identified as significantly upregulated (**Figure 21**). The comparable magnitude of change across both modification states indicates stress-induced upregulation of HSPH1 rather than a redox-driven shift in the oxidation state of Cys13. Oxidation of Cys13, which is flanked by serine and tyrosine residues, could theoretically influence local phosphorylation dynamics through redox-dependent conformational effects,[71] however, the stable ratio between reduced and oxidized forms suggests that the local redox environment at this site was not strongly affected by ATO treatment.

In contrast, the peptide *CQEVISWLDANTLAEK* from HSPA1A, containing Cys574, was detected exclusively in the NEM-modified (reduced) form under control conditions. Following ATO treatment, both NEM- and d5-NEM-modified species were observed, indicating the emergence of an oxidized cysteine population and thus a redox switch at this site (**Figure 20**). In parallel, both modification states increased strongly in intensity, with the reduced fraction showing a ~5.5-fold increase. This peptide was also identified as significantly upregulated in the volcano analysis (**Figure 21**). These findings demonstrate that HSPA1A is markedly induced under ATO stress while Cys574 simultaneously undergoes partial oxidation. Given that Cys574 is located within the substrate-binding domain, this modification is consistent with redox-dependent conformational regulation of HSP70 function.

For HSP8, the peptide *VCNPIITK*, containing Cys603, was detected only in the oxidized form (d5-NEM) under control conditions. Upon ATO treatment, the reduced form became detectable, while the oxidized fraction increased only modestly (~1.7-fold). In the peptide-level analysis no statistically significant regulation was detected. The appearance of a reduced cysteine population may reflect a combination of stress-induced protein turnover introducing newly synthesized reduced HSPA8 and activation of cellular antioxidant systems such as the thioredoxin and glutaredoxin pathways that restore reduced thiols.[72] This observation highlights that redox regulation at individual cysteine sites can be bidirectional and is not restricted to increased oxidation under oxidative stress.

Overall, these examples demonstrate that ATO-induced stress elicits diverse and site-specific cysteine responses within HSP proteins, including induction-dominated effects and partial oxidation or reduction . This heterogeneity highlights the complexity of peptide-level redox regulation.

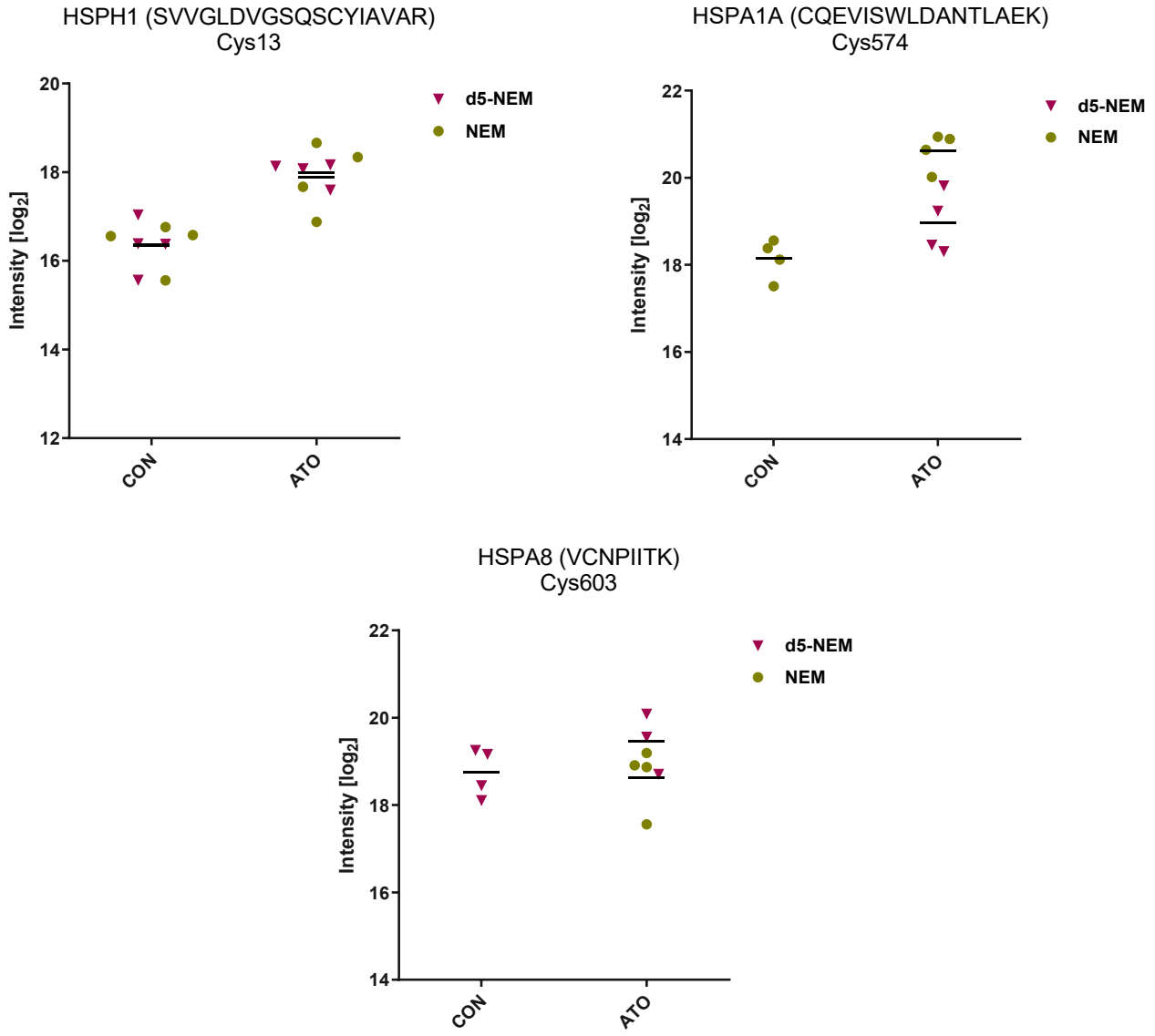

Figure 20: Representative examples of cysteine-containing HSP peptides showing distinct redox and abundance responses to ATO treatment. Log_2 Intensities of NEM- and d5-NEM-modified peptides are shown for HSPH1 Cys13, HSPA1A Cys574, and HSPA8 Cys603 under control and ATO-treated conditions. The examples illustrate induction-dominated regulation (HSPH1), combined induction and redox switching (HSPA1A), and a shift toward a reduced cysteine fraction (HSPA8).

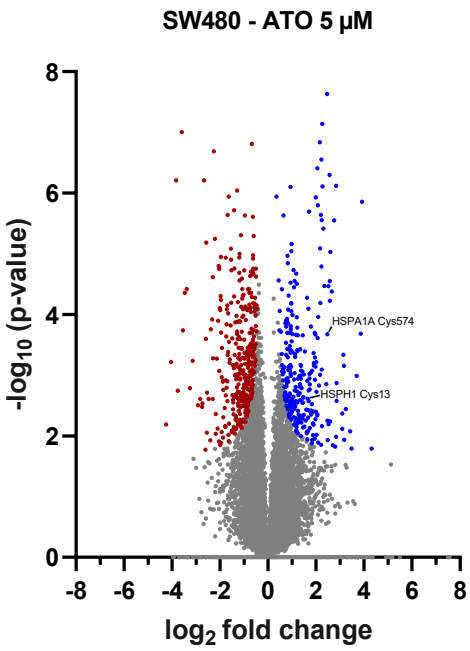

Figure 21: Peptide-level volcano plot of modification-specific peptides in SW480 cells treated with 5 µM ATO. Each data point represents a single NEM- and/or d5-NEM peptide species derived from the modification-specific peptide dataset. No missing-value imputation was applied prior to statistical analysis to avoid artificially introducing peptide intensities that could influence modification-state comparison. Consequently, peptide species detected exclusively in one condition may yield p-values of zero and therefore appear on the x-axis. Red and blue dots represent significantly down- and upregulated peptides, respectively, while grey dots indicate non-significant changes. Highlighted peptides correspond to the HSP peptides discussed in the text (*SVVGLDVGSGSCYIAVAR* from HSPH1 and *CQEVISWLDANTLAEK* from HSPA1A).

4.5.7 Redox specific characterization of HSP and PPP related proteins at the peptide level

To systematically capture diverse peptide-level behaviors across all HSP-derived cysteine-containing peptides, a heatmap-based scoring approach was applied (**Figure 22**). Quantified peptides were evaluated using two metrics: a redox score, reflecting changes in cysteine oxidation state, and an induction score, reflecting changes in peptide abundance. Together, these scores enabled classification of peptide responses as redox-driven, abundance-driven, combined, or unchanged.

For each peptide, the redox score was calculated as the ratio of the NEM/d5-NEM intensity ratio in ATO-treated samples relative to the corresponding ratio in control samples, where $\bar{I}$ denotes average peptide LFQ intensities across biological replicates:

$$redox\ score = \frac{\left(\frac{\bar{I}_{ATO(NEM)}}{\bar{I}_{ATO(d5-NEM)}}\right)}{\left(\frac{\bar{I}_{CON(NEM)}}{\bar{I}_{CON(d5-NEM)}}\right)}$$

Equation 1: Calculation of redox score.

For redox score calculation raw LFQ intensities (not log_2-transformed) were used. The resulting redox score values were subsequently log_2-transformed for visualization and interpretation.

If a peptide was not detected in one modification state, missing values were imputed using fixed low-intensity values (log_2 intensity 11 for NEM and 11.5 for d5-NEM).

The induction score reflects peptide abundance regulation independent of redox state and was calculated from log_2-transformed intensities as the difference between averaged peptide intensities in ATO-treated and control samples, where NEM- and d5-NEM-modified peptide intensities were averaged:

$$induction\ score = \bar{I}_{ATO} - \bar{I}_{CON}$$

Equation 2: Calculation of induction score.

If a peptide was detected exclusively in one condition, fixed values were assigned (+5 for ATO-only detection, -5 for control-only detection), reflecting strong induction or apparent loss of detection under ATO treatment, respectively.

Heatmap visualization

Redox scores (blue scale) and induction scores (yellow-green scale) were visualized in a combined heatmap. White fields indicate peptides for which redox scores could not be calculated because only one modification state was detected in both conditions, or for peptides that were not detected in ATO-treatment.

Peptide-resolved heatmap analysis revealed clear site-specific and bidirectional variability in cysteine redox responses among HSP-associated peptides upon ATO treatment (Figure 22). No uniform shift toward oxidation was observed. Instead, a subset of peptides showed a tendency toward reduction, another subset toward oxidation, while the majority exhibited only minor redox alterations, reflected by the large intermediate blue block.

Induction scores were largely biased toward increased peptide abundance. Notably, peptides assigned an induction score of -5 (control-only detection) frequently corresponded to white fields in the redox score row, as the absence of ATO detection precludes redox score calculation.

Applying a redox score cutoff of $|log_2| \geq 1$, 29% of HSP peptides showed significant redox regulation, of which 16% shifted toward oxidation and 13% toward reduction, supporting the presence of bidirectional and site-specific redox regulation.

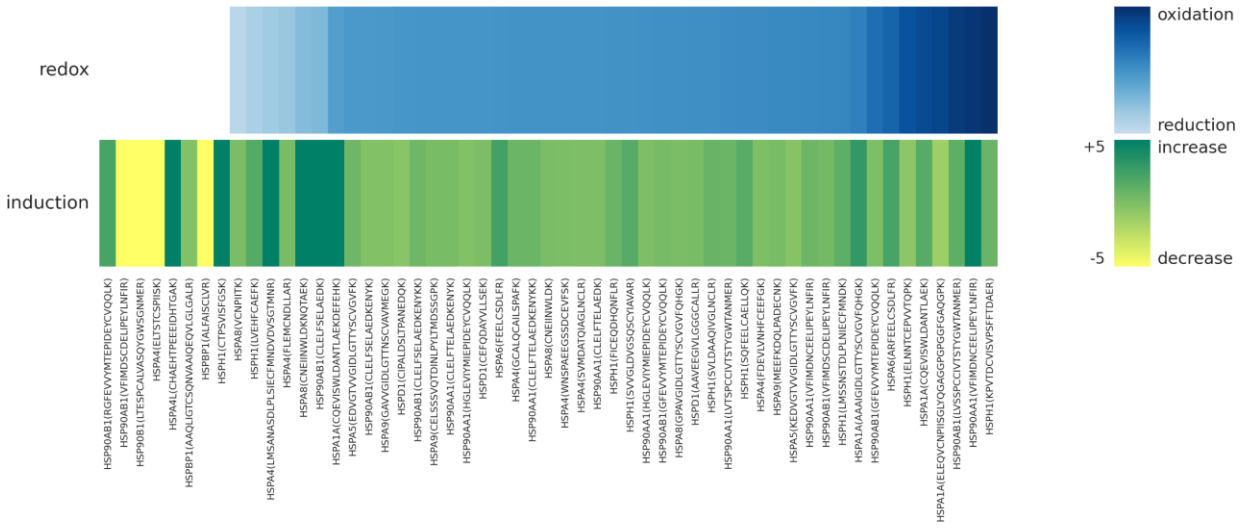

Figure 22: Peptide-resolved redox and induction profiling of cysteine-containing heat shock protein peptides under ATO treatment. Heatmap displays redox scores (blue scale) and induction scores (yellow-green scale) calculated from NEM/d5-NEM-modified peptide intensities. White fields represent peptides for which redox scores could not be calculated or peptides that were not detected in ATO-treated samples.

Given the central role of the pentose phosphate pathway (PPP) in cellular redox homeostasis through NADPH generation, cysteine-containing peptides derived from PPP-associated proteins were subjected to the same redox- and induction- score-based heatmap analysis as described for heat shock proteins (**Figure 24**). The dataset comprised peptides from G6PD, PGLS, PGD, TKT, and TALDO1, enabling pathway-level assessment of redox- and abundance-driven regulation under ATO treatment.

To place the peptide-resolved heatmap results into metabolic context, a schematic representation of the pentose phosphate pathway is shown in **Figure 23.**

The analysed enzymes span both the oxidative (G6PD, PGLS, PGD) and non-oxidative (TKT, TALDO1) branches of the pathway, which together provide ribose-5-phosphate for nucleotide synthesis and, critically, NADPH for cellular antioxidant defense.[73]

G6PD represents the rate-limiting enzyme of the PPP and controls the entry of glucose-6-phosphate into the oxidative branch, thereby determining cellular NADPH production. NADPH serves as a central reducing equivalent required for regeneration of glutathione and thioredoxin systems and is therefore essential for detoxification of reactive oxygen species and maintenance of redox homeostasis.[73]

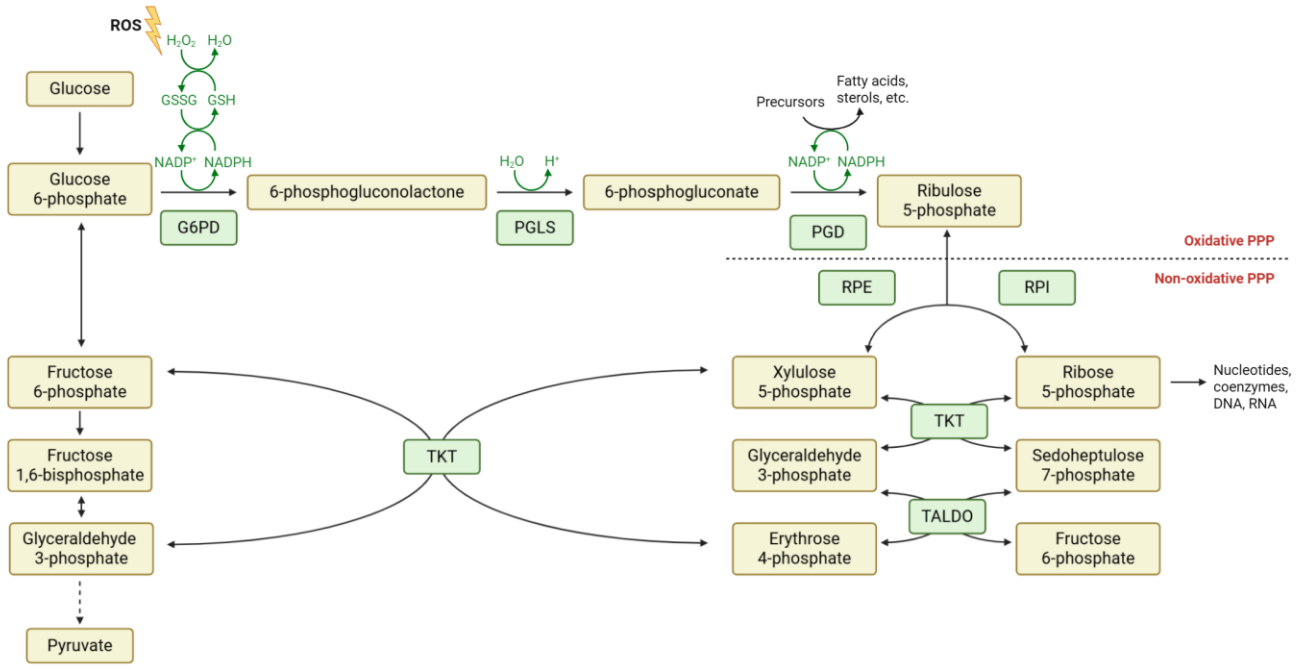

Figure 23: Schematic representation of the pentose phosphate pathway illustrating the positions of analyzed enzymes within the oxidative and non-oxidative branches. Figure created with Biorender, adapted from Ge et al.[73]

Heatmap analysis (**Figure 24**) revealed that cysteine-containing peptides derived from oxidative PPP enzymes exhibited both strong induction and pronounced redox regulation under ATO treatment. G6PD- and PGD-derived peptides showed clear site-specific redox responses, with PGD peptides displaying shifts toward both oxidation and reduction, indicating bidirectional redox regulation. PGLS-derived peptides showed consistent induction with comparatively weak redox shifts, indicating regulation primarily at the level of protein abundance rather than pronounced cysteine redox modulation.

In contrast, peptides derived from the non-oxidative branch enzymes TKT and TALDO1 primarily exhibited induction-dominated responses with comparatively weaker redox shifts, corresponding to largely unchanged NEM/d5-NEM ratios under both control and ATO-treatment. This pattern suggests that flux through the non-oxidative PPP is mainly regulated at the level of protein abundance, whereas cysteine redox regulation is primarily confined to key enzymes of the oxidative branch.

Together, these results support a model in which ATO-induced oxidative stress promotes activation of the pentose phosphate pathway to enhance NADPH production, thereby strengthening cellular antioxidant capacity. While induction of PPP enzymes increases pathway flux, selective cysteine redox regulation provides an additional level of control over enzyme activity during redox stress.

This regulation is particularly important in cancer cell metabolism, where glucose is frequently redirected into the PPP to support NADPH production and redox homeostasis, consistent with metabolic features commonly associated with the Warburg effect.[74]

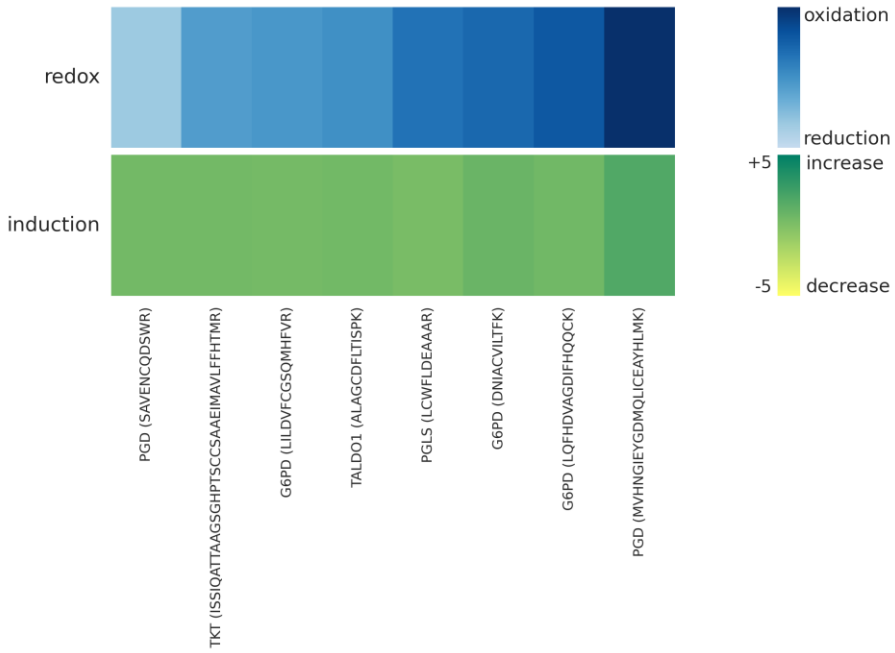

Figure 24: Peptide-resolved redox and induction profiling of pentose phosphate pathway (PPP)-associated proteins under ATO treatment. Heatmap displays redox scores (blue scale) and induction scores (yellow-green scale) calculated from NEM- and d5-NEM-modified cysteine-containing peptides derived from G6PD, PGLS, PGD, TKT, and TALDO1. The upper panel represents redox regulation, with darker blue indicating oxidation and lighter blue indicating reduction, while the lower panel represents peptide abundance regulation.

4.5.8 Limitations

A general limitation of peptide-level redox proteomics is the requirement for consistent detection of the same peptide across biological replicates and experimental conditions. Missing values can reduce statistical power and restrict quantitative comparisons, particularly at the level of individual modification states. Peptides detected exclusively in one condition or modification state prevent direct ratio-based comparisons and necessitate the use of imputation strategies, which may introduce additional uncertainty and reduce quantitative precision.

In addition, peptides may contain multiple potentially modifiable residues, which complicates functional assignment of observed changes to specific regulatory events.

Similar to other PTMs such as phosphorylation, only a small fraction of a given cysteine is expected to be modified at any given time. Thus, redox-modified peptide species often represent only a minor fraction of the total peptide population, limiting detection sensitivity and complicating quantitative interpretation, particularly when protein abundance changes simultaneously.[7,8,75]

Overall, peptide-level redox proteomics provides relative and site-specific insights into redox dynamics rather than absolute measures of modification extent and therefore requires careful interpretation in the context of protein abundance and experimental conditions.

5 Conclusion and Outlook

In this work, a mass spectrometry-based differential alkylation workflow was developed, applied, and critically evaluated for the analysis of cysteine-based redox modifications in cellular systems. The primary objective was to identify parameters describing how comprehensively and reliably the cellular redox proteome can be captured, rather than to provide an exhaustive biological characterization of redox regulation.

Using N-ethylmaleimide (NEM) and isotopically labeled d5-NEM, the established workflow enabled peptide-resolved discrimination between reduced and oxidized cysteine residues. Validation using a defined protein mixture demonstrated the technical feasibility of the approach, while application to fibroblast and colon carcinoma cell lines confirmed its suitability for redox proteome profiling under biologically relevant conditions. Oxidative stress induced by tert-butyl hydroperoxide and arsenic trioxide elicited measurable, site-specific redox responses, illustrating that the method is sensitive to distinct redox perturbations and capable of capturing heterogeneous cysteine behaviours across proteins and pathways.

Analysis at both the protein and peptide levels demonstrated that redox regulation is highly site-specific and cannot be inferred solely from changes in protein abundance. The combined evaluation of redox and induction scores enabled separation of redox-driven effects from abundance-driven regulation and revealed bidirectional cysteine responses under oxidative stress. Application of this strategy to stress-responsive protein networks, including heat shock proteins and pentose phosphate pathway-associated enzymes, showed that redox sensitivity is restricted to defined subsets of regulatory cysteine residues rather than representing a global property of the proteome. These findings illustrate that the workflow can capture biologically interpretable redox signatures relevant to cellular stress adaptation and redox-dependent modes of action.

At the same time, this work highlights important limitations inherent to redox proteomics approaches. Similar to phosphoproteomics, robust quantitative comparison of cysteine redox states relies on consistent detection of the same peptides across biological replicates and experimental conditions. Peptides detected exclusively in one condition or modification state complicate direct ratio-based analyses and necessitate imputation strategies, which may reduce quantitative precision.

Further progress in redox proteomics will depend on advances in data analysis and computational integration. In this work, evaluation of peptide-resolved redox patterns partly relied on manual data processing, reflecting the current lack of standardized bioinformatics pipelines for differential alkylation datasets. Development of dedicated computational frameworks capable of integrating peptide-level modification states, protein abundance changes, and statistical confidence will therefore be important for improving scalability and robustness of redox proteome analyses.

Beyond analytical improvements, integrating redox proteomics with other omics such as phosphoproteomics and metabolomics may help to elucidate how different post-translational modifications interact to shape cellular signaling networks. Such integrative strategies will be essential for translating site-specific redox information into a deeper understanding of the roles of redox-regulation in cellular physiology and disease.

6 References

(1) Almeida, A. J. P. O. de; Oliveira, J. C. P. L. de; Da Silva Pontes, L. V.; Souza Júnior, J. F. de; Gonçalves, T. A. F.; Dantas, S. H.; Almeida Feitosa, M. S. de; Silva, A. O.; Medeiros, I. A. de. ROS: Basic Concepts, Sources, Cellular Signaling, and Its Implications in Aging Pathways. *Oxidative Medicine and Cellular Longevity* 2022, *2022*, 1225578. DOI: 10.1155/2022/1225578.

(2) Juan, C. A.; La Pérez de Lastra, J. M.; Plou, F. J.; Pérez-Lebeña, E. The Chemistry of Reactive Oxygen Species (ROS) Revisited: Outlining Their Role in Biological Macromolecules (DNA, Lipids and Proteins) and Induced Pathologies. *International Journal of Molecular Sciences* 2021, *22* (9). DOI: 10.3390/ijms22094642.

(3) Sies, H.; Belousov, V. V.; Chandel, N. S.; Davies, M. J.; Jones, D. P.; Mann, G. E.; Murphy, M. P.; Yamamoto, M.; Winterbourn, C. Defining Roles of Specific Reactive Oxygen Species (ROS) in Cell Biology and Physiology. *Nature Reviews Molecular Cell Biology* 2022, *23* (7), 499–515. DOI: 10.1038/s41580-022-00456-z.

(4) Thannickal, V. J.; Fanburg, B. L. Reactive Oxygen Species in Cell Signaling. *American Journal of Physiology: Lung Cellular and Molecular Physiology* 2000, *279*, L1005-L1028. DOI: 10.1152/ajplung.2000.279.6.L1005.

(5) Rauf, A.; Khalil, A. A.; Awadallah, S.; Khan, S. A.; Abu-Izneid, T.; Kamran, M.; Hemeg, H. A.; Mubarak, M. S.; Khalid, A.; Wilairatana, P. Reactive Oxygen Species in Biological Systems: Pathways, Associated Diseases, and Potential Inhibitors: A Review. *Food Science & Nutrition* 2024, *12* (2), 675–693. DOI: 10.1002/fsn3.3784.

(6) Kervella, M.; Bertile, F.; Bouillaud, F.; Criscuolo, F. The Cell Origin of Reactive Oxygen Species and Its Implication for Evolutionary Trade-Offs. *Open Biology* 2025, *15* (4), 240312. DOI: 10.1098/rsob.240312.

(7) Go, Y.-M.; Jones, D. P. The Redox Proteome. *The Journal of Biological Chemistry* 2013, *288* (37), 26512–26520. DOI: 10.1074/jbc.R113.464131.

(8) Li, X.; Gluth, A.; Zhang, T.; Qian, W.-J. Thiol Redox Proteomics: Characterization of Thiol-Based Post-Translational Modifications. *Proteomics* 2023, *23* (13-14), e2200194. DOI: 10.1002/pmic.202200194.

(9) Knoke, L. R.; Leichert, L. I. Global Approaches for Protein Thiol Redox State Detection. *Current Opinion in Chemical Biology* 2023, *77*, 102390. DOI: 10.1016/j.cbpa.2023.102390.

(10) Lennicke, C.; Rahn, J.; Heimer, N.; Lichtenfels, R.; Wessjohann, L. A.; Seliger, B. Redox Proteomics: Methods for the Identification and Enrichment of Redox-Modified Proteins and Their Applications. *Proteomics* 2016, *16* (2), 197–213. DOI: 10.1002/pmic.201500268.

(11) Anjo, S. I.; He, Z.; Hussain, Z.; Farooq, A.; McIntyre, A.; Laughton, C. A.; Carvalho, A. N.; Finelli, M. J. Protein Oxidative Modifications in Neurodegenerative Diseases: From Advances in Detection and Modelling to Their Use as Disease Biomarkers. *Antioxidants* 2024, *13* (6), 681. DOI: 10.3390/antiox13060681.

(12) Rudzińska, M.; Parodi, A.; Balakireva, A. V.; Chepikova, O. E.; Venanzi, F. M.; Zamyatnin, A. A. Cellular Aging Characteristics and Their Association with Age-Related Disorders. *Antioxidants* 2020, *9* (2). DOI: 10.3390/antiox9020094.

(13) Han, X.; Aslanian, A.; Yates, J. R. Mass Spectrometry for Proteomics. *Current Opinion in Chemical Biology* 2008, *12* (5), 483–490. DOI: 10.1016/j.cbpa.2008.07.024.

(14) Bantscheff, M.; Lemeer, S.; Savitski, M. M.; Kuster, B. Quantitative Mass Spectrometry in Proteomics: Critical Review Update From 2007 to the Present. *Analytical and Bioanalytical Chemistry* 2012, *404* (4), 939–965. DOI: 10.1007/s00216-012-6203-4.

(15) Roberg-Larsen, H.; Wilson, S. R.; Lundanes, E. Recent Advances in On-Line Upfront Devices for Sensitive Bioanalytical Nano LC Methods. *Trends in Analytical Chemistry* 2021, *136*, 116190. DOI: 10.1016/j.trac.2021.116190.

(16) Wilson, S. R.; Vehus, T.; Berg, H. S.; Lundanes, E. Nano-LC in Proteomics: Recent Advances and Approaches. *Bioanalysis* 2015, *7* (14), 1799–1815. DOI: 10.4155/bio.15.92.

(17) Juraschek, R.; Dülcks, T.; Karas, M. Nanoelectrospray-More Than Just a Minimized-Flow Electrospray Ionization Source. *Journal of the American Society for Mass Spectrometry* 1999, *10* (4), 300–308. DOI: 10.1016/S1044-0305(98)00157-3.

(18) Laskay, Ü. A.; Lobas, A. A.; Srzentić, K.; Gorshkov, M. V.; Tsybin, Y. O. Proteome Digestion Specificity Analysis for Rational Design of Extended Bottom-Up and Middle-Down Proteomics Experiments. *Journal of Proteome Research* 2013, *12* (12), 5558–5569. DOI: 10.1021/pr400522h.

(19) Meyer, J. G. Qualitative and Quantitative Shotgun Proteomics Data Analysis from Data-Dependent Acquisition Mass Spectrometry. *Methods in Molecular Biology* 2021, *2259*, 297–308. DOI: 10.1007/978-1-0716-1178-4_19.

(20) Fernández-Costa, C.; Martínez-Bartolomé, S.; McClatchy, D. B.; Saviola, A. J.; Yu, N.-K.; Yates, J. R. Impact of the Identification Strategy on the Reproducibility of the DDA and DIA Results. *Journal of Proteome Research* 2020, *19* (8), 3153–3161. DOI: 10.1021/acs.jproteome.0c00153.

(21) Guan, S.; Taylor, P. P.; Han, Z.; Moran, M. F.; Ma, B. Data Dependent-Independent Acquisition (DDIA) Proteomics. *Journal of Proteome Research* 2020, *19* (8), 3230–3237. DOI: 10.1021/acs.jproteome.0c00186.

(22) Zhang, F.; Ge, W.; Huang, L.; Li, D.; Liu, L.; Dong, Z.; Xu, L.; Ding, X.; Zhang, C.; Sun, Y.; A, J.; Gao, J.; Guo, T. A Comparative Analysis of Data Analysis Tools for Data-Independent Acquisition Mass Spectrometry. *Molecular & Cellular Proteomics* 2023, *22* (9), 100623. DOI: 10.1016/j.mcpro.2023.100623.

(23) Zhao, L.; Cong, X.; Zhai, L.; Hu, H.; Xu, J.-Y.; Zhao, W.; Zhu, M.; Tan, M.; Ye, B.-C. Comparative Evaluation of Label-Free Quantification Strategies. *Journal of Proteomics* 2020, *215*, 103669. DOI: 10.1016/j.jprot.2020.103669.

(24) Zhu, W.; Smith, J. W.; Huang, C.-M. Mass Spectrometry-Based Label-Free Quantitative Proteomics. *Journal of Biomedicine & Biotechnology* 2010, *2010*, 840518. DOI: 10.1155/2010/840518.

(25) Cox, J.; Hein, M. Y.; Luber, C. A.; Paron, I.; Nagaraj, N.; Mann, M. Accurate Proteome-Wide Label-Free Quantification by Delayed Normalization and Maximal Peptide Ratio Extraction, Termed MaxLFQ. *Molecular & Cellular Proteomics* 2014, *13* (9), 2513–2526. DOI: 10.1074/mcp.M113.031591.

(26) Meier, F.; Beck, S.; Grassl, N.; Lubeck, M.; Park, M. A.; Raether, O.; Mann, M. Parallel Accumulation-Serial Fragmentation (PASEF): Multiplying Sequencing Speed and Sensitivity by Synchronized Scans in a Trapped Ion Mobility Device. *Journal of Proteome Research* 2015, *14* (12), 5378–5387. DOI: 10.1021/acs.jproteome.5b00932.

(27) Meier, F.; Park, M. A.; Mann, M. Trapped Ion Mobility Spectrometry and Parallel Accumulation-Serial Fragmentation in Proteomics. *Molecular & Cellular Proteomics* 2021, *20*, 100138. DOI: 10.1016/j.mcpro.2021.100138.

(28) Bruker. *CaptiveSpray*. https://www.bruker.com/en/products-and-solutions/mass-spectrometry/ion-sources/captivespray.html (accessed 2026-01-25).

(29) Meier, F.; Brunner, A.-D.; Koch, S.; Koch, H.; Lubeck, M.; Krause, M.; Goedecke, N.; Decker, J.; Kosinski, T.; Park, M. A.; Bache, N.; Hoerning, O.; Cox, J.; Räther, O.; Mann, M. Online Parallel Accumulation-Serial Fragmentation (PASEF) with a Novel Trapped Ion Mobility Mass Spectrometer. *Molecular & Cellular Proteomics* 2018, *17* (12), 2534–2545. DOI: 10.1074/mcp.TIR118.000900.

(30) Wojdyla, K.; Rogowska-Wrzesinska, A. Differential Alkylation-Based Redox Proteomics-Lessons Learnt. *Redox Biology* 2015, *6*, 240–252. DOI: 10.1016/j.redox.2015.08.005.

(31) Cuddihy, S. L.; Baty, J. W.; Brown, K. K.; Winterbourn, C. C.; Hampton, M. B. Proteomic Detection of Oxidized and Reduced Thiol Proteins in Cultured Cells. *Methods in Molecular Biology* 2009, *519*, 363–375. DOI: 10.1007/978-1-59745-281-6_23.

(32) Thermo Fisher Scientific. *N-Ethylmaleimide (NEM)*:*User Guide*. https://documents.thermofisher.com/TFS-Assets/LSG/manuals/MAN0011563_NEthylmaleimide_NEM_UG.pdf (accessed 2026-02-01).

(33) Getz, E. B.; Xiao, M.; Chakrabarty, T.; Cooke, R.; Selvin, P. R. A Comparison between the Sulfhydryl Reductants Tris(2-carboxyethyl)phosphine and Dithiothreitol for Use in Protein Biochemistry. *Analytical Biochemistry* 1999, *273* (1), 73–80. DOI: 10.1006/abio.1999.4203.

(34) Leichert, L. I.; Gehrke, F.; Gudiseva, H. V.; Blackwell, T.; Ilbert, M.; Walker, A. K.; Strahler, J. R.; Andrews, P. C.; Jakob, U. Quantifying Changes in the Thiol Redox Proteome upon Oxidative Stress in Vivo. *Proceedings of*

the National Academy of Sciences of the United States of America 2008, *105* (24), 8197–8202. DOI: 10.1073/pnas.0707723105.

(35) Thermo Fisher Scientific. Introduction to Thiol Modification and Detection. In *Molecular Probes Handbook*:*A Guide to Fluorescent Probes and Labeling Technologies,* 11th ed., 2010.

(36) Kenyon, G. L.; DeMarini, D. M.; Fuchs, E.; Galas, D. J.; Kirsch, J. F.; Leyh, T. S.; Moos, W. H.; Petsko, G. A.; Ringe, D.; Rubin, G. M.; Sheahan, L. C. Defining the Mandate of Proteomics in the Post-Genomics Era: Workshop Report. *Molecular & Cellular Proteomics* 2002, *1* (10), 763–780. DOI: 10.1016/S1535-9476(20)34374-7.

(37) Topf, U.; Suppanz, I.; Samluk, L.; Wrobel, L.; Böser, A.; Sakowska, P.; Knapp, B.; Pietrzyk, M. K.; Chacinska, A.; Warscheid, B. Quantitative Proteomics Identifies Redox Switches for Global Translation Modulation by Mitochondrially Produced Reactive Oxygen Species. *Nature Communications* 2018, *9* (1), 324. DOI: 10.1038/s41467-017-02694-8.

(38) Thermo Fisher Scientific. *Iodoacetyl Tandem Mass Tag (iodoTMT) Reagents*:*User Guide*. https:// documents.thermofisher.com/TFS-Assets/LSG/manuals/MAN0011795_Iodoacetyl_TandemMassTag_ iodoTMT_Reag_UG.pdf (accessed 2026-01-25).

(39) Saei, A. A.; Gullberg, H.; Sabatier, P.; Beusch, C. M.; Johansson, K.; Lundgren, B.; Arvidsson, P. I.; Arnér, E. S. J.; Zubarev, R. A. Comprehensive Chemical Proteomics for Target Deconvolution of the Redox Active Drug Auranofin. *Redox Biology* 2020, *32*, 101491. DOI: 10.1016/j.redox.2020.101491.

(40) Kučera, O.; Endlicher, R.; Roušar, T.; Lotková, H.; Garnol, T.; Drahota, Z.; Cervinková, Z. The Effect of tert-Butyl Hydroperoxide-Induced Oxidative Stress on Lean and Steatotic Rat Hepatocytes in Vitro. *Oxidative Medicine and Cellular Longevity* 2014, *2014*, 752506. DOI: 10.1155/2014/752506.

(41) Brozek-Pluska, B.; Beton, K. Oxidative Stress Induced by tBHP in Human Normal Colon Cells by Label Free Raman Spectroscopy and Imaging. The Protective Role of Natural Antioxidants in the Form of β-Carotene. *RSC Advances* 2021, *11* (27), 16419–16434. DOI: 10.1039/d1ra01950c.

(42) Bortel, P.; Hagn, G.; Skos, L.; Bileck, A.; Paulitschke, V.; Paulitschke, P.; Gleiter, L.; Mohr, T.; Gerner, C.; Meier-Menches, S. M. Memory Effects of Prior Subculture May Impact the Quality of Multiomic Perturbation Profiles. *Proceedings of the National Academy of Sciences of the United States of America* 2024, *121* (29), e2313851121. DOI: 10.1073/pnas.2313851121.

(43) Jambrovics, K.; Póliska, S.; Scholtz, B.; Uray, I. P.; Balajthy, Z. ATO Increases ROS Production and Apoptosis of Cells by Enhancing Calpain-Mediated Degradation of the Cancer Survival Protein TG2. *International Journal of Molecular Sciences* 2023, *24* (13). DOI: 10.3390/ijms241310938.

(44) Kumar, S.; Yedjou, C. G.; Tchounwou, P. B. Arsenic Trioxide Induces Oxidative Stress, DNA Damage, and Mitochondrial Pathway of Apoptosis in Human Leukemia (HL-60) Cells. *Journal of Experimental & Clinical Cancer Research* 2014, *33* (1), 42. DOI: 10.1186/1756-9966-33-42.

(45) Birner-Gruenberger, R.; Tomin, T.; Honeder, S.; Liesinger, L.; Gremel, D.; Retzl, B.; Lindenmann, J.; Brcic, L.; Schittmayer, M. *Active Oxidative Metabolism and Impaired Glyoxalase System Under Increased Intracellular Oxidative Stress in Non-Small Cell Lung Cancer*, 2024. DOI: 10.21203/rs.3.rs-4535848/v1.

(46) Hoehlschen, J.; Gosset, É.; Hofreither, D.; Jahnel, S.; Mendjan, S.; Schittmayer, M.; Tomin, T.; Birner-Gruenberger, R. Heart Saver: Comprehensive Investigation of (Redox-) Proteomic and Thiol Metabolite Changes Induced by Cana-, Dapa-, Empagliflozin Treatment in 2D and 3D Heart Cell Models Reveals Increased Mitochondrial Activity and Glutathione Redox Defense and Involvement of Redox Signaling. *Life Sciences* 2025, *380*, 123923. DOI: 10.1016/j.lfs.2025.123923.

(47) Ghasemi, M.; Turnbull, T.; Sebastian, S.; Kempson, I. The MTT Assay: Utility, Limitations, Pitfalls, and Interpretation in Bulk and Single-Cell Analysis. *International Journal of Molecular Sciences* 2021, *22* (23). DOI: 10.3390/ijms222312827.

(48) Madelaire, C. B.; Klink, A. C.; Israelsen, W. J.; Hindle, A. G. Fibroblasts as an Experimental Model System for the Study of Comparative Physiology. *Comparative Biochemistry and Physiology Part B: Biochemistry and Molecular Biology* 2022, *260*, 110735. DOI: 10.1016/j.cbpb.2022.110735.

(49) Wang, Y.; Tang, Q.; Jiang, S.; Li, M.; Wang, X. Anti-Colorectal Cancer Activity of Macrostemonoside A Mediated by Reactive Oxygen Species. *Biochemical and Biophysical Research Communications* 2013, *441* (4), 825–830. DOI: 10.1016/j.bbrc.2013.10.148.

(50) Spolaore, B.; Bermejo, R.; Zambonin, M.; Fontana, A. Protein Interactions Leading to Conformational Changes Monitored by Limited Proteolysis: Apo Form and Fragments of Horse Cytochrome C. *Biochemistry* 2001, *40* (32), 9460–9468. DOI: 10.1021/bi010582c.

(51) Thermo Fisher Scientific. *TCEP-HCl*:*User Guide*. https://documents.thermofisher.com/TFS-Assets/LSG/manuals/MAN0011306_TCEP_HCl_UG.pdf (accessed 2026-02-04).

(52) Ngo, V.; Duennwald, M. L. Nrf2 and Oxidative Stress: A General Overview of Mechanisms and Implications in Human Disease. *Antioxidants* 2022, *11* (12). DOI: 10.3390/antiox11122345.

(53) Petrache, I.; Otterbein, L. E.; Alam, J.; Wiegand, G. W.; Choi, A. M. Heme Oxygenase-1 Inhibits TNF-alpha-Induced Apoptosis in Cultured Fibroblasts. *American Journal of Physiology: Lung Cellular and Molecular Physiology* 2000, *278* (2), L312-L319. DOI: 10.1152/ajplung.2000.278.2.L312.

(54) Jeong, W.; Bae, S. H.; Toledano, M. B.; Rhee, S. G. Role of Sulfiredoxin as a Regulator of Peroxiredoxin Function and Regulation of Its Expression. *Free Radical Biology and Medicine* 2012, *53* (3), 447–456. DOI: 10.1016/j.freeradbiomed.2012.05.020.

(55) Tonelli, C.; Chio, I. I. C.; Tuveson, D. A. Transcriptional Regulation by Nrf2. *Antioxidants & Redox Signaling* 2018, *29* (17), 1727–1745. DOI: 10.1089/ars.2017.7342.

(56) Jain, A.; Rusten, T. E.; Katheder, N.; Elvenes, J.; Bruun, J.-A.; Sjøttem, E.; Lamark, T.; Johansen, T. p62/Sequestosome-1, Autophagy-related Gene 8, and Autophagy in Drosophila Are Regulated by Nuclear Factor Erythroid 2-related Factor 2 (NRF2), Independent of Transcription Factor TFEB. *The Journal of Biological Chemistry* 2015, *290* (24), 14945–14962. DOI: 10.1074/jbc.M115.656116.

(57) Kerins, M. J.; Ooi, A. The Roles of NRF2 in Modulating Cellular Iron Homeostasis. *Antioxidants & Redox Signaling* 2018, *29* (17), 1756–1773. DOI: 10.1089/ars.2017.7176.

(58) Zhang, H.; Gong, W.; Wu, S.; Perrett, S. Hsp70 in Redox Homeostasis. *Cells* 2022, *11* (5). DOI: 10.3390/cells11050829.

(59) Stein, S.; Thomas, E. K.; Herzog, B.; Westfall, M. D.; Rocheleau, J. V.; Jackson, R. S.; Wang, M.; Liang, P. NDRG1 is Necessary for p53-Dependent Apoptosis. *The Journal of Biological Chemistry* 2004, *279* (47), 48930–48940. DOI: 10.1074/jbc.M400386200.

(60) Rong, M.-H.; Li, J.-D.; Zhong, L.-Y.; Huang, Y.-Z.; Chen, J.; Xie, L.-Y.; Qin, R.-X.; He, X.-L.; Zhu, Z.-H.; Huang, S.-N.; Zhou, X.-G. CCNB1 Promotes the Development of Hepatocellular Carcinoma by Mediating DNA Replication in the Cell Cycle. *Experimental Biology and Medicine* 2022, *247* (5), 395–408. DOI: 10.1177/15353702211049149.

(61) Wu, J.; Chen, M.; Peng, Z.; Sun, Y.; Jin, J. Mechanism and Research Progress of MAPK Signaling Pathway in Myocardial Fibrosis. *Frontiers in Cardiovascular Medicine* 2025, *12*, 1667568. DOI: 10.3389/fcvm.2025.1667568.

(62) Andor, A.; Mohanraj, M.; Pató, Z. A.; Úri, K.; Biri-Kovács, B.; Cheng, Q.; Arnér, E. S. J. TXNL1 Has Dual Functions as a Redox Active Thioredoxin-Like Protein as Well as an ATP- and Redox-Independent Chaperone. *Redox Biology* 2023, *67*, 102897. DOI: 10.1016/j.redox.2023.102897.

(63) O'Connor, L.; Gilmour, J.; Bonifer, C. The Role of the Ubiquitously Expressed Transcription Factor Sp1 in Tissue-specific Transcriptional Regulation and in Disease. *The Yale Journal of Biology and Medicine* 2016, *89* (4), 513–525.

(64) Christmann, M.; Kaina, B. Epigenetic Regulation of DNA Repair Genes and Implications for Tumor Therapy. *Mutation Research: Reviews in Mutation Research* 2019, *780*, 15–28. DOI: 10.1016/j.mrrev.2017.10.001.

(65) Peng, M.; Xie, J.; Ucher, A.; Stavnezer, J.; Cantor, S. B. Crosstalk between BRCA-Fanconi Anemia and Mismatch Repair Pathways Prevents MSH2-Dependent Aberrant DNA Damage Responses. *The EMBO Journal* 2014, *33* (15), 1698–1712. DOI: 10.15252/embj.201387530.

(66) Duong, L. D.; West, J. D.; Morano, K. A. Redox Regulation of Proteostasis. *The Journal of Biological Chemistry* 2024, *300* (12), 107977. DOI: 10.1016/j.jbc.2024.107977.

(67) Yang, J.; Zhang, H.; Gong, W.; Liu, Z.; Wu, H.; Hu, W.; Chen, X.; Wang, L.; Wu, S.; Chen, C.; Perrett, S. S-Glutathionylation of Human Inducible Hsp70 Reveals a Regulatory Mechanism Involving the C-Terminal α-

Helical Lid. *The Journal of Biological Chemistry* 2020, *295* (24), 8302–8324. DOI: 10.1074/jbc.RA119.012372.

(68) Miyata, Y.; Rauch, J. N.; Jinwal, U. K.; Thompson, A. D.; Srinivasan, S.; Dickey, C. A.; Gestwicki, J. E. Cysteine Reactivity Distinguishes Redox Sensing by the Heat-Inducible and Constitutive Forms of Heat Shock Protein 70. *Chemistry & Biology* 2012, *19* (11), 1391–1399. DOI: 10.1016/j.chembiol.2012.07.026.

(69) Prodromou, C. Mechanisms of Hsp90 Regulation. *The Biochemical Journal* 2016, *473* (16), 2439–2452. DOI: 10.1042/BCJ20160005.

(70) Nardai, G.; Sass, B.; Eber, J.; Orosz, G.; Csermely, P. Reactive Cysteines of the 90-kDa Heat Shock Protein, Hsp90. *Archives of Biochemistry and Biophysics* 2000, *384* (1), 59–67. DOI: 10.1006/abbi.2000.2075.

(71) Su, Z.; Burchfield, J. G.; Yang, P.; Humphrey, S. J.; Yang, G.; Francis, D.; Yasmin, S.; Shin, S.-Y.; Norris, D. M.; Kearney, A. L.; Astore, M. A.; Scavuzzo, J.; Fisher-Wellman, K. H.; Wang, Q.-P.; Parker, B. L.; Neely, G. G.; Vafaee, F.; Chiu, J.; Yeo, R.; Hogg, P. J.; Fazakerley, D. J.; Nguyen, L. K.; Kuyucak, S.; James, D. E. Global Redox Proteome and Phosphoproteome Analysis Reveals Redox Switch in Akt. *Nature Communications* 2019, *10* (1), 5486. DOI: 10.1038/s41467-019-13114-4.

(72) Sies, H.; Berndt, C.; Jones, D. P. Oxidative Stress. *Annual Review of Biochemistry* 2017, *86*, 715–748. DOI: 10.1146/annurev-biochem-061516-045037.

(73) Ge, T.; Yang, J.; Zhou, S.; Wang, Y.; Li, Y.; Tong, X. The Role of the Pentose Phosphate Pathway in Diabetes and Cancer. *Frontiers in Endocrinology* 2020, *11*, 365. DOI: 10.3389/fendo.2020.00365.

(74) Qiao, Y.; Liu, Y.; Ran, R.; Zhou, Y.; Gong, J.; Liu, L.; Zhang, Y.; Wang, H.; Fan, Y.; Fan, Y.; Nan, G.; Zhang, P.; Yang, J. Lactate Metabolism and Lactylation in Breast Cancer: Mechanisms and Implications. *Cancer and Metastasis Reviews* 2025, *44* (2), 48. DOI: 10.1007/s10555-025-10264-4.

(75) Olsen, J. V.; Mann, M. Status of Large-Scale Analysis of Post-Translational Modifications by Mass Spectrometry. *Molecular & Cellular Proteomics* 2013, *12* (12), 3444–3452. DOI: 10.1074/mcp.O113.034181.

7 Appendix

Table 14: List of used materials and devices

Material List

- Cell Medium: Minimum Essential Medium Eagle (MEM) [*Sigma-Aldrich*, LOT: RNBN0625] (+50 mL 10% FBS [*gibco*, LOT: B2741830 RP], + 5 mL Pen Strep, *Sigma-Aldrich*, LOT: 215793])
- Trypsin: StableCell™ Trypsin Solution [*Sigma-Aldrich*]
- MTT salt: Thiazolyl Blue Tetrazolium Bromide [*Sigma-Aldrich*, CAS-No.: 298-93-1, PCode: 1003699373, Source: MKCS4540]
- PBS (sterile filtered): prepared in-house from 4 salts as 10x concentrated solution: (80x NaCl, 2x KCl, 14.4x $Na_2HPO_4 \cdot 2H_2O$, 2.8 g KH_2PO_4) in 1L H_2O; 1x PBS is prepared from this 10x PBS stock solution
- SDC-Buffer: Sodium deoxycholate [*Sigma*, CAS: 302-96-4, LOT: BCCD1238]
- 2M Tris-HCl pH 8.5
- ABC buffer, ammonium bicarbonate [*Sigma-Aldrich*, CAS: 1066-33-7, Sigma Aldrich, LOT: BCBS2121V]
- Tert-Butyl hydroperoxide solution (TBHP) [*Sigma Aldrich*, CAS: 75-91-2, 458, LOT: BCCB8820, 458139-25 mL]
- Arseinc(III) oxide (As_2O_3), [*Sigma-Aldrich*, CAS: 1327-53-3, 202673-5G, LOT: MKBQ6516V]
- IL-1 beta human, recombinant [*Sigma Aldrich*, LOT: VB24040404]
- Tris(2-carboxyethyl)phosphine hydrochloride (TCEP) [*Sigma-Aldrich*, CAS-No: 51805-45-99, PCode 1003504503, Source SLCJ7305]
- N-Ethylmaleimide (NEM) [*Sigma Aldrich*, CAS-No: 128-53-0, PCode 102822395, Source BCCM2997]
- N-Ethyl-d5-maleimide (d5-NEM) [*Sigma Aldrich*, CAS-No: 380768-37-2, 692905-10MG, PCode 1003730652, Source MBBD9176]
- Promega Mass Spec Grade Trypsin/LysC Mix 20 µg [*Fisher Scientific*, LOT: 0000611722]
- Promega Resuspension Buffer:(100% AcOH, $CaCl_2$, H_2O) [*Fisher Scientific*]
- Ubiquitin from bovine erythrocytes [*Sigma*, U6253-25MG, LOT: SLBR6351V]
- Cytochrome c from equine heart [*Sigma* C7752-100MG, LOT: SLBJ8107V]
- Albumin from human serum, [*Sigma* A3782-100MG,LOT: SLBT8667]
- Recombinant HsTRXR1 (TXNRD1), CAT: HTRXR1-5, Selenozyme, LOT: HTRXR1221220
- Dimethyl sulfoxide (DMSO), puriss. P.a., dried [*Sigma-Aldrich*, CAS: 67-68-5, LOT: STBL0407]
- Styrenedivinylbenzene revervse phase sulfonate (SDB-PRS): Empore 2241 SDB-RPS, 12 µm particle size, 47 mm; CDS Analytical LLC
- SDB-PRS Loading and wash buffer 1 (TFA 1% in IPA)
- SDB-PRS Loading and wash buffer 2 (ACN 5%, TFA 0.2% in VWR water)
- SDB-PRS Elution buffer (ACN 60%, VWR water 40%, NH_3 0.0014%)
- Ammonium hydroxide solution, 28% NH_3 in H_2O [*Sigma Aldrich*, LOT: SHBB0317V]
- MS-Loading TIMS-ToF buffer (ACN, TFA, VWR water)
- VWR-H_2O

Device List

- VivaSpin® 500 µL, 3 kDa MWCO cut off filter [*Sartorius*]
- Scraper: Sarstedt AG & Co. KG
- Centrifuges: *Thermo Scientific*, Megafuge 168 and Heraeus Megafuge 16R; *Eppendorf*, Centrifuge 5425 R
- Water bath: *Huber*, KISS 118A

- Incubator cell culture: *Thermo Scientific*, CO_2 Incubator Heracell 150i
- Waste: Integra Vacusafe
- CellDrop™ BF, DeNOVIX
- Plate reader: MULTISKAN GO Microplate Spectrophotometer, Thermo Scientific
- Thermoshaker: *Eppendorf* ThermoMixer C and *Eppendorf* Thermomixer comfort
- SpeedVac: GeneVac miVac Duo concentrator
- Ultrasonicator: *Bandelin* Sonorex Digital 10 P
- Ultrasonic Stick: *Bandelin*, device for settings: *Bandelin* Sonoplus
- pH meter: *inoLAB*, WTW series, Terminal 740
- Microscope: *ZEISS* Primo Vert with AxioCamERc5s
- Microscope software for visualizing: ZEN (blue editicion), 2006-2011 Carl Zeiss MicroImaging
- Plate reading software: SkanIt RE for Multiskan GO 3.2
- Autosampler: Thermo scientific Dionex UltiMate 3000 RS Autosampled UHPLC+ focused
- LC: *Thermo Scientific*, Dionex UltiMate 3000 RSCLnano System
- MS: *Bruker* timsTOF Pro (powered by PASEF)
- Used software: Perseus 1.6.14, GraphPadPrism 8.0.1, Venny 2.1, ChemDraw 23.0.1
- Used websites: string-db.org, davidbioinformatics.nih.gov, biorender.com, uniprot.org

Abbreviations

ABC	Ammonium bicarbonate
ACC	Acceleration
Alb	Albumin
AP-1	Activator protein-1
ATO	Arsenic trioxide
AUC	Area under the curve
BCA	Bicinchoninic acid
CO_2	Carbon dioxide
CON	Control
C-peptide	Cysteine-containing peptide
CSNK1A1	Casein kinase I isoform alpha
CSNK2A2	Casein kinase II subunit alpha'
Cys	Cysteine
CytC	Cytochrome c
DDA	Data dependent acquisition
DEC	Deceleration
DIA	Data independent acquisition
DMSO	Dimethyl sulfoxide
DNA	Desoxyribonucleic acid
DNMT1	DNA methyltransferase 1
DTT	Dithiothreitol
EDTA	Ethylenediaminetetraacetic acid
FANCD2	Fanconi anemia complementation group D2 protein
FBS	Fetal bovine serum
FDR	False discovery rate
FOS	Fos proto-oncogene, AP-1 transcription factor subunit (c-Fos)
FOSL1	Fos-related antigen 1
FOSL2	Fos-related antigen 2
FTL	Ferritin light chain
G6PD	Glucose-6-phosphate dehydrogenase
GCLM	Glutamate-cysteine ligase modifier subunit
GSH	Glutathione
GSSG	Glutathione disulfide
H_2O	Water
H_2O_2	Hydrogen peroxide
HMOX1	Heme oxygenase-1
HSP	Heat shock protein
IAM	Iodoacetamide
IC	Inhibitory concentration

IC_{50}	Half maximal inhibitory concentration
ICAT	Isotope-coded affinity tag
IL-1β	Interleukin-1 beta
JUN	Jun proto-oncogene, AP-1 transcription factor subunit (c-Jun)
KCl	Potassium chloride
KEAP1	Kelch-like ECH-associated protein 1
KH_2PO_4	Potassium dihydrogen phosphate
LC	Liquid chromatography
LFQ	Label-free quantification
LysC	Lysyl endopeptidase
m/z	Mass to charge ratio
MAPK	Mitogen-activated protein kinase
MEM	Minimum Essential Medium
MS	Mass spectrometry
MSH2	DNA mismatch repair protein MSH2
MTT	3-(4,5-Dimethylthiazol-2-yl)-2,5-diphenyltetrazolium bromide
Na_2HPO_4	Sodium hydrogen phosphate
NaCl	Sodium chloride
NADPH	Nicotinamide adenine dinucleotide phosphate
nanoLC	Nano liquid chromatography
NaOH	Sodium hydroxide
NBD	Nucleotide-binding domain
NEM	N-ethylmaleimide
NF-κB	Nuclear factor kappa-light-chain-enhancer of activated B cells
NH_4OH	Ammonium hydroxide
NRF2	Nuclear factor erythroid 2-related factor 2
OxICAT	Oxidation-dependent isotope-coded affinity tag
oxPTM	Oxidative post-translational modifications
p53	Tumor protein p53
PASEF	Parallel accumulation-serial fragmentation
PBS	Phosphate-buffered saline
PenStrep	Penicillin-streptomycin
PGD	6-Phosphogluconate dehydrogenase
PGLS	6-Phosphogluconolactonase
PML-RARα	Promyelocytic leukaemia protein-retinoic acid receptoralpha
PPP	Pentose phosphate pathway
PTM	Post-translational modifications
QTOF	Quadrupole time-of-flight
redox	Reduction-oxidation
ROS	Reactive oxygen species
RP	Reversed phase

rpm	Rounds per minute
RT	Room temperature
SBD	Substrate-binding domain
SD	Standard deviation
SDC	Sodium deoxycholate
SP1	Transcription factor SP1
SPAG9	C-Jun-amino-terminal kinase-interacting protein 4
SQSTM1	Sequestome-1
SRXN1	Sulfiredoxin-1
TALDO	Transaldolase
TBHP	tert-Butyl hydroperoxide
TCEP	Tris(2-carboxyethyl)phosphine
TCP1	T-complex protein 1 subunit alpha
tims	Trapped ion mobility mass spectrometer
TKT	Transketolase
TMT	Tandem mass tags
TNFRSF10B	Tumor necrosis factor receptor superfamily member 10B
TNFRSF10D	Tumor necrosis factor receptor superfamily member 10D
TOF	Time-of-flight
TXNL1	Thioredoxin-like protein 1
TXNRD1	Thioredoxin reductase 1
Ubi	Ubiquitin
v/v	Volume per volume

In the course of this thesis, the AI-based tools DeepL and ChatGPT were used for language improvement and stylistic editing. In addition, Python scripts used for visualization of selected graphs were reviewed and refined with the assistance of ChatGPT.